The HPXPS Instrument at MAX-lab: A Powerful Tool for *In Situ* Catalysis Investigations

MASTER THESIS IN PHYSICS

AUTHOR: NICLAS JOHANSSON

SUPERVISORS: JAN KNUDSEN AND JOACHIM SCHNADT

DIVISON OF SYNCHROTRON RADIATION RESEARCH
LUND UNIVERSITY

To be presented at a public seminar in room H422 at the department of Physics in Lund May 31, 2012.

Populärvetenskaplig sammanfattning

I dagens samhälle används diverse katalysatorer i många sammanhang för att påskynda kemiska reaktioner. Allt från produktion av ammoniak till rening av avgaser hjälps av olika katalysatorer. De katalysatorer som vi känner idag har tagits fram genom att testa olika materialkombinationer och utvecklingen har börjat stagnera.

Enzymerna i våra kroppar är naturliga katalysatorer. Vid jämförelse av enzymers och industriella katalysatorers effektivitet framkommer det att det bör finnas möjlighet till stora förbättringar utav de konstgjorda katalysatorerna. För att förbättra dagens katalysatorer krävs ingående kunskaper på atomär nivå angående de reaktionsmekanismer som ligger bakom de katalytiska prosesserna. Dessa processer har under förra seklet studerats med bl.a. röntgenfotoelektronspektroskopi (XPS), och då nästan uteslutande i ultrahögvakuum (UHV).

Det har uppdagats att de strukturer och mekanismer som funnits vid UHV-studierna inte nödvändigvis motsvarar de strukturer och förutsättningar som uppkommer i de verkliga katalysatorerna. Anledningen till detta är det stora tryckgapet mellan UHV och en verklig katalysators tryckbetingelser: industriella katalysatorer, som arbetar typiskt i atmosfärs- eller ännu högre tryck. För att brygga detta tryckgap har högtrycks-XPS (HPXPS) utvecklats. Idag finns det ett antal HPXPS-instrument vid diverse synkrotronljusanläggningar runtom i världen, men de saknar förmågan att snabbt byta mellan högt tryck och UHV. Här rapporteras utformningen av ett HPXPS-instrument som kan just detta.

Det nya HPXPS-instrumentet vid MAX IV-laboratoriet är utrustat med en liten flyttbar kammare inuti det stora vakuumsystemet. Denna kammare tillåter att högtrycksexperiment utförs i en begränsad volym, medan det övriga systemet hålls under UHV. Med denna utformning tillåts ett byte mellan UHV-mätningar i vakuumkammaren och högtrycksmätningar inuti den lilla kammaren, och en länk mellan tidigare UHV-studier och nya högtrycksexperiment erhålls.

Med hjälp av instrumentet undersöktes CO-oxidationen över en platinayta. Instrumentet kunde detektera reaktanterna, CO och O_2, i gasfasen samt på platinaytan. Produkten, CO_2 detekterades i gasfasen genom både XPS och masspektrometri. På platinaytan växtes även en ultratunn järnoxidfilm bestående av två atomära lager som sedan oxiderades i 0,5 mbar O_2 till en film med tre lager. Oxidationen följdes *in situ* med HPXPS vilket inte har

rapporterats om tidigare. Dessa experiment påvisar möjligheten hos HPXPS-instrumentet att följa katalysreaktioner vid förutsättningar som efterliknar de verkliga katalysatorerna vilket medför att kunskap angående de bakomliggande atomära processerna kan fås. Förhoppningen är att HPXPS därmed kan bidra till en utveckling av mycket effektiva specialdesignade katalysatorer för alla användningsområden utifrån "första principer".

Abstract

A new instrument for near ambient x-ray photoelectron spectroscopy investigations of surfaces has been installed at beamline I511 of the MAX-II electron storage ring at the MAX IV Laboratory. This high pressure x-ray photoelectron spectroscopy instrument is capable of surface chemistry investigations in near ambient pressures using x-ray photoelectron spectroscopy (XPS), a technique that traditionally is limited to ultrahigh vacuum.

To test the instrument, a trilayer iron oxide film was grown with O_2 pressures in the mbar regime. The growth was monitored *in situ* with XPS, an experiment which is not found in the literature. The XPS fingerprint of the trilayer FeO_2 film was characterised in UHV, and consists of two major peaks in the O 1s spectrum and the peaks were assigned to its respective O species.

The oxidation of CO over Pt(111) surface was also investigated using the HPXPS instrument. The oxidation process was observed with a quadrupole mass spectrometer in coincidence with the *in situ* XPS measurements, showing the possibility to measure reactivity using the setup.

In this thesis, the basics of the experiment methods are presented and the high pressure instrument is described in detail. Further, the structures and growth of the different FeO films are discussed on the basis of my own XPS and low energy electron diffraction (LEED) results and the data available in the literature.

Preface

This paper is a master thesis in physics written at the Division of Synchrotron Radiation Research at Lund University. The author is a student of the master program in physics at the natural science faculty.

I would like to give my sincerest gratitude to Jan Knudsen and Joachim Schnadt for inviting me to participate in this project. Further, I would like to thank them both for good cooperation when installing the instrument. Also, for the encouragement and good advice during the process of writing this thesis. Additional people deserving thanks for setting up the instrument are Annette Pietzsch, Anders Olsson and additional staff at the MAX IV Laboratory. Furthermore, I would like to thank Søren Porsgaard for the help during the beamtimes.
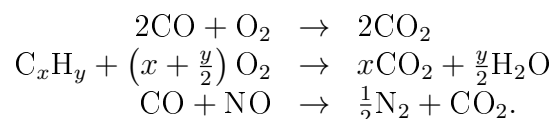
Contents

1. Introduction

Catalysts are ubiquitous and heavily affect our daily lives. For example, enzymes, the natural catalysts in our and all mammals' bodies, make life sustaining reactions possible, and their importance is self-evident. Another extremely important catalytic process is the so-called Haber-Bosch process in which NiO is used as a catalyst to synthesise ammonia. Without this process, large-scale production of artificial fertiliser would be impossible and a world population larger than 3 billion would be difficult to sustain [1]. Therefore, the Haber-Bosch process is by many considered to be the most important invention of the 20th century. In recognition of their achievements, Fritz Haber and Carl Bosch were awarded with the Nobel Prize in 1918 and 1931, respectively [2,3]. Further, Gerhard Ertl was awarded with the Nobel Prize in 2007 for his studies of chemical reactions on surfaces, in particular in relationship to the Haber-Bosch process [4].

Although the above mentioned catalysts are very important, the most widely known catalyst is the automotive three-way catalyst in which CO, hydrocarbons (C_xH_y) and NO_x are oxidised or reduced in three simultaneous reactions:

$$
\begin{aligned}
2CO + O_2 &\rightarrow 2CO_2 \\
C_xH_y + \left(x + \tfrac{y}{2}\right)O_2 &\rightarrow xCO_2 + \tfrac{y}{2}H_2O \\
CO + NO &\rightarrow \tfrac{1}{2}N_2 + CO_2.
\end{aligned}
$$

Here the catalyst is used to convert toxic species(CO, C_xH_y, NO_x) into less harmful molecules (CO_2, H_2O, N_2). A typical three-way catalyst is based on Pt and Rh particles, where Pt catalyses the two oxidation reactions, while Rh catalyses the NO reduction. The car catalyst is an excellent example of an environmentally important catalyst.

Essentially all the catalysts we know today have been developed by *trial and error* methods and development has begun to stagnate. However, given that many artificial catalysts are less effective than enzymes, improvement should be possible. Therefore catalysts developed and based on an understanding of the catalytic processes on an atomic level is desired. Further, an

understanding of the chemistry behind the catalytic processes could improve efficiency and create more durable catalysts.

Heterogeneous Catalysis

From the above examples, the importance of understanding catalysis is evident. A catalyst is defined as a substance which increases reaction rates without being consumed. As a result, the temperature at which a non-zero reaction rate is observed is lowered significantly, and it becomes possible to run the reaction at much lower temperatures with the catalyst present. The reason for the increased reaction rate is the introduction of a new reaction pathway, which lowers the overall energy barrier as illustrated in Figure 1.1.

There are many different catalysts and they are sorted into two major groups. If the catalyst and reactant are in the same phase, e.g. in the liquid phase, it is a *homogeneous* catalyst. If the reactants and catalyst are in different phases, e.g. if the catalyst is solid and the reactants gaseous, it is called a *heterogeneous* catalyst. Heterogeneous catalysts are preferred by the chemical industry as they make separation of the catalyst and product fairly easy.

Different catalysts work in different ways. Three different processes are illustrated in Figure 1.1. In panel (a) the Langmuir-Hinshelwood mechanism is illustrated and the overall process can be summed up in four steps. First the reactants are adsorbed onto the surface. The adsorbed molecules then diffuse on the surface and react as the reactants meet. The newly formed molecule desorbs. The dashed line shows the reaction path for the gas phase and thus illustrates the difference in energy barriers between the catalysed and non-catalysed reaction paths. Another important mechanism is the Eley-Rideal mechanism where one molecule adsorbs onto the surface and the reaction takes place when the other hits it from the gas phase as illustrated in Figure 1.1(b). Panel (c) shows the Mars-van Krevelen mechanism where gas phase molecules react with the surface, leaving it reduced.

The surface science approach

Many catalysts are composed of precious metals which make them expensive. Therefore, in practical applications, the catalyst materials are often dispersed as particles on a porous support to reduce material amounts and also to increase the surface area. This makes for a complex system which is difficult
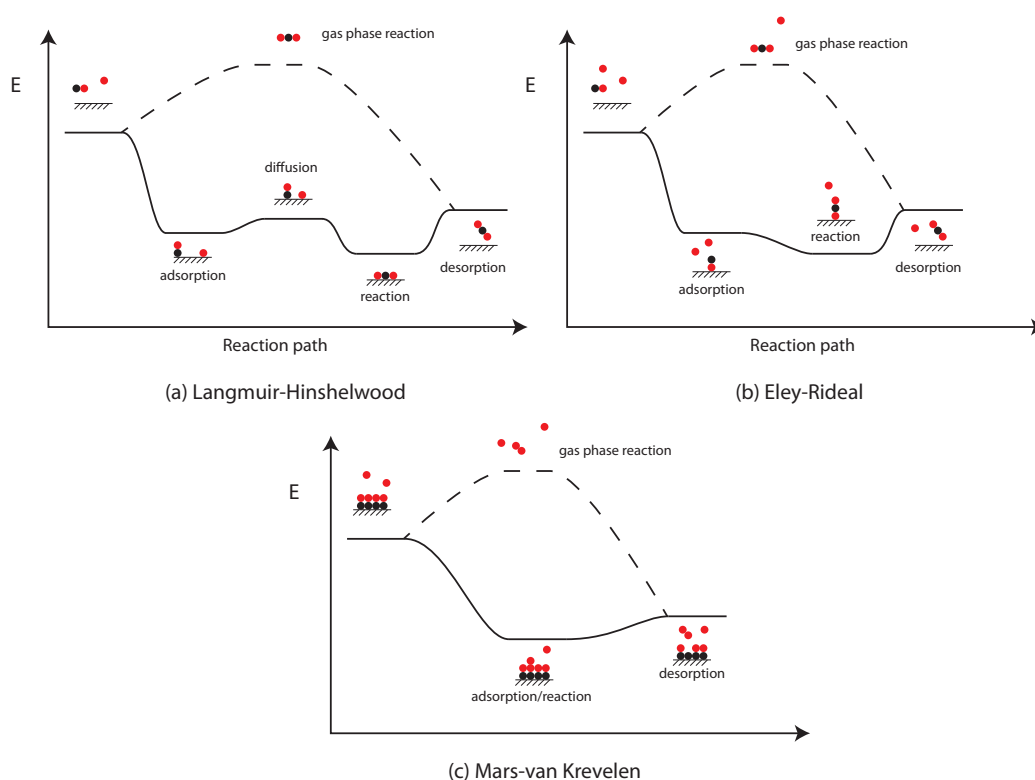
Fig. 1.1: Energy diagram as function of reaction path for three catalysis mechanisms.

to study on an atomic scale. In order to gain knowledge of the atomic inter-
actions, the systems under study need to be simplified. The surface science
approach is to use single crystal surfaces in a strictly controlled environment,
usually in ultrahigh vacuum (UHV). Using these simplified systems in ultra-
high vacuum it becomes possible to conduct very controlled experiments and
gain fundamental knowledge of atomic interactions. However, real catalysts
are quite far from single crystals and usually operate in pressures above 1
bar. This has lead to the introduction of the concepts of a *material gap* and
a *pressure gap*. The material gap refers to the difference in structural com-
plexity between single crystal surfaces and real catalysts, while the pressure
gap refers to the vast difference in pressure. During recent years, the need
to bridge these gaps has become evident. For example, studies have shown
that the atomic structures in UHV can be different from those formed at
ambient pressures [5–7], but there are also indications that some structures
are identical in UHV and at ambient pressures [8].

Near ambient pressure spectroscopy

UHV conditions are not only far from reality, but their use heavily restricts the choice of sample. Due to this, Siegbahn et al. [9] developed a differentially pumped gas cell for x-ray photoelectron spectroscopy (XPS) already in the late 1960s. During the following years, the first dedicated XPS instruments for liquids [10] and surfaces immersed in vapours [11] were developed. The field of high pressure x-ray photoelectron spectroscopy (HPXPS) - where 'high pressure' refers to the vast pressure difference between UHV and near ambient conditions - slowly developed [12–15] during the late 20th century, and with the introduction of third generation synchrotron radiation sources the development of HPXPS reached a breakthrough. The increased photon intensity allowed higher pressures as the photoelectron flux increased to a point where the electron loss due to inelastic scattering became less significant. Moreover, groups at two synchrotron radiation facilities, the ALS and BESSY, developed a differentially pumped electrostatic lens system, which significantly increased the transmission through their analysers [16–18].

This thesis

The need for more efficient catalysts based on the knowledge of chemical reactions on an atomic scale has increased the demand for *in situ* studies in near ambient conditions. Here I report on the installation of a new HPXPS system which has been installed at the MAX IV Laboratory. It should be noted that since the instrument is placed at a national laboratory, external research groups can apply for beamtime to conduct various studies. A picture of the system is shown in Figure 1.2.

The system itself was built by SPECS GmbH partly based on an idea from Lund [19]. In my diploma work, I have been heavily involved in the mounting and testing of this new instrument; it will therefore be described in detail. Additionally, the installation of the instrument has lead to the submission of a paper to the Journal of Synchrotron Radiation [19]. To test the new instrument, a newly found surface film relevant for catalysis, the trilayer iron oxide, was studied *in situ*. In addition, adsorption and reactivity on a Pt(111) crystal was also investigated.

During the course of my practical work with the instrument, I also developed three different programs for the instrument using the programming suite LabVIEW. The first of these programs is capable of reading the pressures from all the different chambers of the instrument and logging them in a
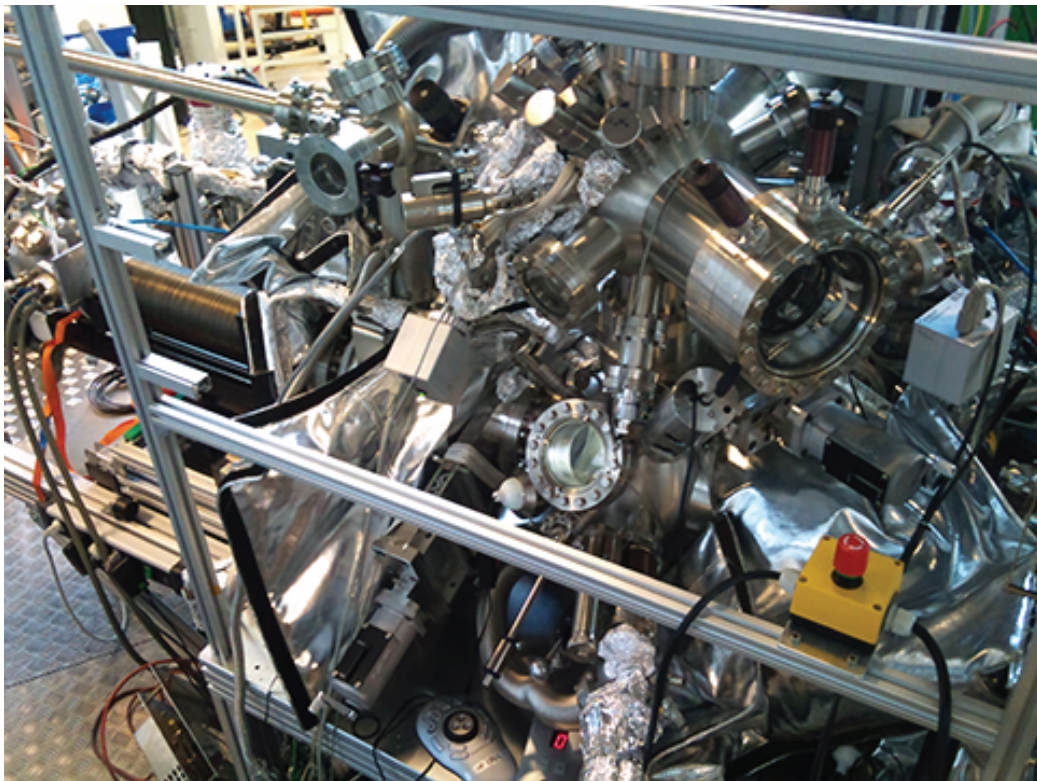
Fig. 1.2: A picture of the instrument. The preparation chamber and LEED apparatus is clearly visible in the middle of the image.

textfile for further analysis. The second program is built for logging the pressure in the 11 different dry scrolling pumps. The last program reads and sets the temperature for the heating in the high pressure cell.

In Chapter 2 I will present the basic principles for the two surface science techniques employed. The instrument itself will be described in Chapter 3. The three following chapters describe the model systems used and measurement results. In the last chapter, I will conclude and give a short outlook.

2. Experimental Methods

Surface science employs many different techniques, e.g. surface x-ray diffraction, x-ray absorption spectroscopy, and photoemission electron microscopy. In the following chapter, I will give the basic theory and present the experimental principles for the two main techniques employed, x-ray photoelectron spectroscopy and low energy electron diffraction.

2.1 X-ray Photoelectron Spectroscopy

The photoelectric effect was discovered by H. Hertz in 1887 [20], and the phenomenon was explained by A. Einstein in 1905 [21]. This explanation awarded Einstein the Noble Prize in physics in 1921. The photoelectric effect is illustrated in Figure 2.1, where a surface hit by a photon emits an electron. Photoelectron spectroscopy (PES) emerged from the discovery of the photoelectric effect and it has proved to be one of the most versatile techniques for studying surface chemistry. When using x-rays, PES is often referred to as x-ray photoelectron spectroscopy (XPS) and thus XPS will be used to denote the technique in this work.

The mean free path of electrons

Electrons interact strongly with matter, meaning that they can travel only short distances before they loose energy. The average distance electrons can travel before loosing energy is called the *inelastic mean free path* (IMFP) and is typically a few Å for electrons in solids. As the IMFP in solids is comparable with the thickness of atomic layers, electron based techniques are very surface sensitive. The length of the IMFP depends on the energy of the electrons and the medium trough which it is travels.

The attenuation of electrons travelling through matter is given by [22]

$$I(x) = I_0 e^{-x/\mu}, \tag{2.1}$$

where x is the travelled distance, μ is the *attenuation length* of the electrons and I_0 the intensity at $x = 0$. In contrast to the IMFP, μ also includes elastic scattering making IMFP exceed μ by about 10-30% [23, 24]. As an example, the IMFP for 100 eV electrons in a solid Pt sample is 4.15 Å and the interatomic distance of Pt(111) is $\sim$2.7 Å. From Eq.(2.1) it is thus clear that two layers of Pt are enough to attenuate the electron flux by approximately 50%, if elastic scattering is neglected.

The short IMFP that makes XPS very surface sensitive unfortunately also makes it difficult to detect photoelectrons from a solid sample immersed in a gas atmosphere in a conventional XPS setup. Usually, the electrons need to travel quite large distance, $\sim$1 m, in order to be detected. For electrons of $E_k = 400$ eV, the IMFP in 1 mbar O_2 is about 4 mm [25], meaning that no electrons would be detected after travelling 1 m according to Eq. (2.1). Therefore, experiments are usually performed in high vacuum (P $<10^{-6}$ mbar) in order to see electrons. Actually, in surface science UHV (P $\approx 10^{-10}$ mbar) is prefered to protect the detector, as it should not exceed 10^{-7} mbar, and to keep the surface clean, which is important due to the surface sensitivity of XPS. A surface immersed in an atmosphere of 10^{-6} mbar will be covered by one monolayer of gas molecules in one second, if it is assumed that the sticking coefficient is one. In contrast, the same sample can be kept clean for nearly three hours at 10^{-10} mbar.
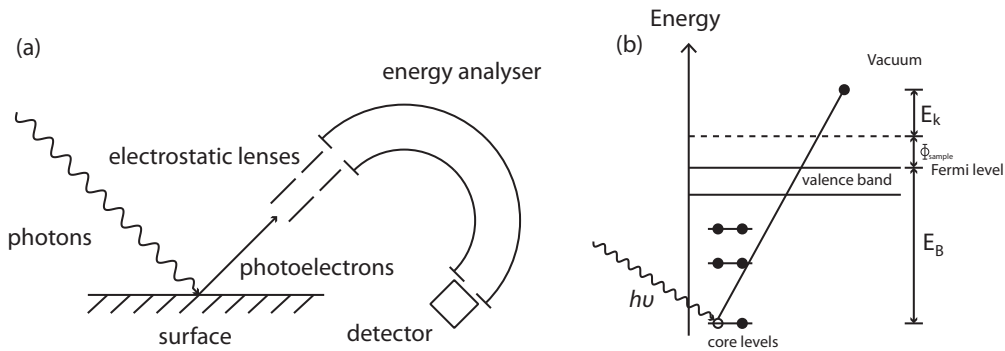

Fig. 2.1: Principle of XPS. (a) schematic drawing of a XPS experiment is shown. (b) energy level diagram of the process.

XPS principles

An illustration of an XPS experiment is shown in Figure 2.1(a). A photon hits a surface and a *photoelectron* is emitted as a result of the photoelectric effect. The photoelectron is then collected in an electron energy analyser. Typically, a hemispherical electron energy analyser is used, as seen in the figure, but other types exist [22]. The hemispherical energy analyser works as a bandpass filter, i.e. only electrons with a certain energy, $E \pm \Delta E$, can pass through and be detected. ΔE is the resolution of the hemisphere, which is analyser-specific and adjustable. The energy electrons must have in order to pass through is called the pass energy, E_{pass}, which is usually held constant during spectrum acquisition. As the resolution is coupled to the pass energy, the resolution will be independent of the kinetic energy of the photoelectrons. To acquire a spectrum, a retarding or accelerating field is applied by an electrostatic lens system. This will change the kinetic energy of the photoelectrons, and by sweeping the applied voltage a complete spectrum is acquired. As both the applied field and the pass energy are known, the initial kinetic energy of the photoelectron can be calculated. Additionally, the electrostatic lenses focus the angularly dispersed electrons, thereby increasing the overall transmission.

In Figure 2.1(b), an energy level diagram of the XPS process is shown and it can be explained by the three step model [22]:

1. The electron is excited by the incoming photon.

2. The excited electron is transported to the surface.

3. The electron penetrates trough the vacuum barrier and becomes a free electron with kinetic energy E_k.

The photoelectrons are then collected, as described above, and their kinetic energy is analysed. The core levels do not participate in the bonding between atoms and therefore x-ray photoelectron (XP) spectra contain element-specific features [26].

The kinetic energy of the photoelectron can be calculated by using the energy conservation principle

$$E_i + h\nu = E_f + E_k, \tag{2.2}$$

where $h\nu$ is the energy of the incoming photon, E_k is the kinetic energy of the outgoing electron, E_i and E_f are the initial and final state energies of the system, respectively. By rearrangement of Eq.(2.2) the kinetic energy is

found to be

$$E_k = h\nu - (E_f - E_i). \tag{2.3}$$

The difference in energy between the final and initial state, i.e. the neutral atom and the ion, is called the ionisation potential. In XPS it is useful to have the Fermi energy as reference as it can be measured. Therefore the ionisation potential is equal to the binding energy of the electron plus the surface work function. Then Eq.(2.3) becomes

$$E_k = h\nu - (E_B + \Phi), \tag{2.4}$$

where E_B is the binding energy and Φ is the work function of the surface. During an experiment, the surface and detector are connected, so that their Fermi levels are aligned. Also, as the measured kinetic energy is the kinetic energy in the analyser, Φ in Eq.(2.4) becomes the analyser work function instead of the sample work function.

XP spectrum analysis

The particular example of a C 1s XP spectrum of styrene ($C_6H_5CH{=}CH_2$) adsorbed on AgO clusters is shown in Figure 2.2. In the following I will discuss how to analyse such a spectrum. When analysing the XPS data, the important parameters are

- the binding energy,

- the peak area,

- the peak width, and

- the background.

As binding energies are element-specific, it is straightforward to identify elements on the surface using XPS. Therefore, absolute binding energies are often not that relevant. Instead, the so-called *chemical shifts* are of utmost importance. A chemical shift is a shift in electron binding energy induced by a change in the chemical environment of the photoemitting atom. Figure 2.2 provides an example. Styrene is a molecule which consists of a benzene ring with an ethene derivative. Thus styrene contains two different C atoms which are seen as two components in the XP spectrum. The component marked ethene originates from the two C atoms in the ethene derivative, while the component marked benzene originates from the six C atoms in the benzene ring. As a result, molecules can be identified by looking at the relative binding energy between their respective components, and this
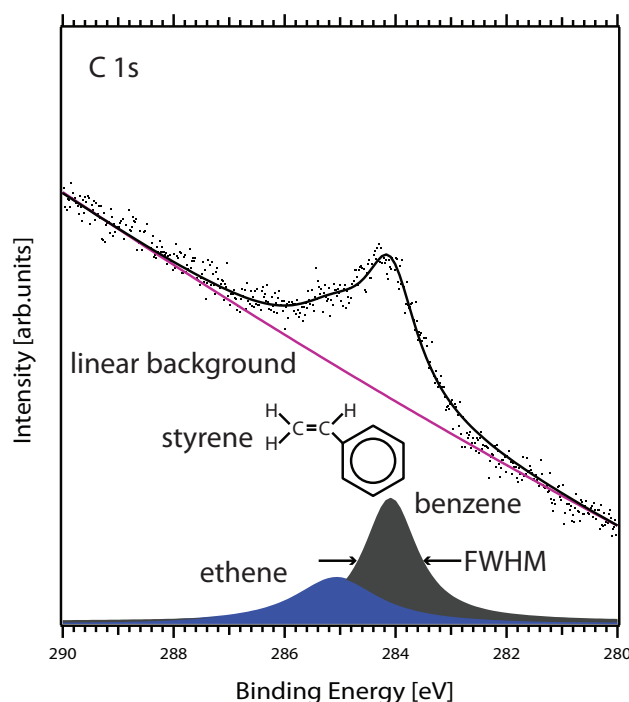
Fig. 2.2: A C 1s spectrum of of 100 L styrene dosed onto AgO clusters supported by an 1 ML FeO(111) film on a Pt(111) substrate.

is why the technique is sometimes called *Electron Spectroscopy for Chemical Analysis* (ESCA).

XPS is also a quantitative technique, meaning that the amount of collected photoelectrons is proportional to the amount of probed atoms. Therefore, by comparing peak areas, the relative concentration of species can be found, which is clearly seen in the figure. The peak component attributed to benzene has a greater area, which is expected as there are more C atoms in the benzene ring than in the ethene derivative. However, the *photoionisation cross section* needs to be considered when comparing XP spectra measured with different photon energies. The cross section varies with photon energy and therefore it is not always straightforward to conduct quantitative analyses of XP spectra. Additionally, the photoionisation cross section needs to be considered when choosing photon energy in order to gain maximum count rates during experiments. Therefore, the cross sections have been measured by previous groups and can, for example, be found in [27].

The width of an XPS peak is determined by a number of factors; the main factors are the natural linewidth and instrumental broadening, i.e. photon energy and detector broadening. The natural linewidth is determined by

the lifetime of the core-excited state according to Heisenberg's uncertainty principle. As an example, the natural linewidth of Pt 4f is typically ~ 0.35 eV [28]. The photon energy broadening is determined by the excitation source. In synchrotron facilities, a monochromator is used to obtain monochromatic light. The resolution of the light will then be given by the size of the exit slit, while the detector broadening is determined by the pass energy. Typical values for monochromator and analyser resolutions are 0.05 eV and 0.02 eV, respectively. However, the photon energy and analyser broadening heavily depends on the experimental setup. The width of peaks are measured at half maximum to obtain the so-called *full width at half maximum* (FWHM).

Often XPS peaks look asymmetric due to the spectral background. Therefore, background subtraction is an important aspect of XPS analysis. By looking at the data points in Figure 2.2, it looks like there is a tail towards lower binding energy. However, after subtraction of a linear background, two symmetric components are found. The background itself is mainly composed of two parts. Screening of the core hole leading to the creation of electron-hole pairs and excitations of plasmons and other quantised secondary excitations [29] create a tail on the high binding energy side, likewise the inelastic scattering of the outgoing photoelectrons [30] creates a background. The linear background in Figure 2.2 is due to inelastic scattering of XPS lines with lower binding energy. Both the screening and inelastic scattering effects are asymmetric and create a background which is higher on the high binding energy side. This is normally accounted for by a so-called *Shirley* background [31] which determines the background iteratively. Other commonly used backgrounds are linear or polynomial backgrounds. The background subtraction is phenomenological and thus strongly depends on the surface. However, quantitative models exist, e.g. the *Tougaard* background [32], but are not used in this thesis.

To find the binding energy, area and width of each XPS component, theoretical functions are fitted to the peaks. The function to be used depends on the data, but in general, the lineshape is chosen which represents the data best. In XP spectra where the lifetime dominates the broadening, a Lorentzian function is an appropriate estimation of the line shape [33]. The Lorentzian function is expressed as

$$L(E) = \frac{1}{\pi} \frac{\frac{1}{2}\Gamma_L}{(E - E_0)^2 + \left(\frac{1}{2}\Gamma_L\right)^2}, \tag{2.5}$$

where Γ_L is the FWHM of the function and E_0 is the peak centre. An example of a Lorentz function is shown in Figure 2.3. In XPS data where

instrumental effects dominate the broadening, a Gauß profile is used [33]. The Gauß function is expressed as

$$G(E) = Ie^{-\left(\frac{(E-E_0)}{\Gamma_G}\right)^2},\tag{2.6}$$

where I is the peak maximum, E_0 the peak centre and Γ_G the FWHM. An example of a Gauß function can be seen in Figure 2.3. The true lineshape often contains contributions from both lifetime and instrumentation broadening. Therefore, a convolution of a Gaußian and a Lorentzian may be used, the so-called *Voigt* function [33], which is expressed as

$$V(E) = G(E) * L(E) = \int G(E')L(E - E')dE'.\tag{2.7}$$

An example of a Voigt profile is shown in Figure 2.3. Sometimes it is useful to have asymmetric line profiles to fit to the XPS peaks but the Voigt function is symmetric by definition. Such an asymmetric lineshape may be modelled by combining two half Voigt functions with different widths, which renders the line asymmetric toward the high energy side.
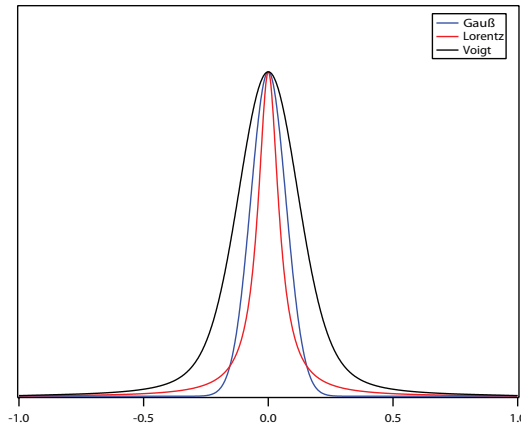

Fig. 2.3: Examples of a Lorentz,Gauß and Voigt profile

Experiments have shown that XP spectra of metallic atoms very often are strongly asymmetric towards the high energy side. This is due to the creation of excited hole-electron pairs in the conduction band of the metal [29]. This excitation creates an excited final state and the kinetic energy of the photoelectron is reduced. A lineshape, which takes into account this effect, was given by Doniach and Šunjić [29]. It is parametrised as follows:

$$Y(\epsilon) = \frac{\Gamma(1-\alpha)}{(\epsilon^2 + \gamma^2)^{(1-\alpha)/2}} \cos\left[\frac{\pi\alpha}{2} + \theta(\epsilon)\right]\tag{2.8}$$

with

$$\theta(\epsilon) = (1 - \alpha)\tan^{-1}(\epsilon/\gamma), \qquad (2.9)$$

where Γ is the gamma function, 2γ is the FWHM of the Lorentzian shape and α is an asymmetry parameter. The Doniach-Šunjić lineshape has a Lorentzian shape and an asymmetry corresponding to the one found in metallic systems. In order to fit the function to experiment data, the Doniach-Šunjić function is convoluted with a Gaußian to accommodate in particular for instrumental broadening. This method has been successfully employed on metallic systems and works well. However, it has been reported that the Doniach-Šunjić function does not represent the lineshape of platinum peaks [34]. Therefore, the platinum peaks in my experiments were fitted by the use of asymmetric Voigt functions on a constant background. For the other core levels, asymmetric Voigt functions were also employed, but with varying backgrounds.

2.2 Low Energy Electron Diffraction

Since its introduction in the 1960s, Low Energy Electron Diffraction (LEED) has been a very important technique for surface structure analysis. LEED makes use of elastically backscattering of low energy electrons with an energy in the range of 20 to 2000 eV. The technique is very surface sensitive due to the short mean free path of electrons in condensed matter, as discussed above. Indeed, prior to the invention and commercial availability of the scanning tunnelling microscope (STM), LEED was the main technique for surface structure analysis. In 1991, i.e. around the time that the STM became commercially available, approximately 40% [35] of all previous surface structure analysis had been done by LEED. LEED is still a very useful technique for structural analysis due to its versatility, simplicity, and time-effective use. Therefore the HPXPS instrument is equipped with a LEED apparatus for *ex situ* structural characterisation. Further, the LEED gives users a possibility to compare surface structures prepared in vacuum chamber at the HPXPS instrument with surface structures prepared in their home laboratories.

Wave nature of particles

Particles behaves like waves and their wavelengths are given by the de Broglie equation

$$\lambda = \frac{h}{p},$$ (2.10)

where λ is the wavelength, h is Planck's constant and p is the momentum of the particle. For electrons, the de Broglie equation can be written as [26]

$$\lambda[\text{Å}] = \left(\frac{150.6}{E[\text{eV}]}\right)^{\frac{1}{2}}.$$ (2.11)

The wavelengths obtained from Eq.(2.11) are in the range of 2.74-0.388 Å for electrons with kinetic energies between 20 eV and 1000 eV, respectively. Theses wavelengths correspond to the interatomic distances in solids and molecules, making diffraction possible. As mentioned earlier, the mean free path for electrons in condensed matter is short for electrons, below 10 Å [35] at low kinetic energies. Due to the short mean free path, electrons travel only a few atomic layers inside a solid without loosing energy. Like XPS, LEED is therefore a surface sensitive technique.

LEED instrumentation

In Figure 2.4 a schematic image of a LEED apparatus is shown. An electron gun is used to produce electrons with a given kinetic energy. The electrons scatter on the sample and are reflected towards a fluorescent screen. Before reaching the screen, the electrons need to pass a series of grids. The grids repel inelastically scattered electrons, and thus only elastic scattering are detected. The first grid is grounded, ensuring that the electrons travel in a field free environment. The grid nearest to the screen is also grounded to shield the **E**-field from the voltage on the screen. The middle grid is held at a negative potential to serve as an energy filter. The high voltage put on the screen will accelerate the elastically scattered electrons, which have passed the grids, to high energies, to ensure that light is emitted. The grid side of the screen is covered with indium tin oxide (ITO), and the fluorescence is produced by a P43 cadmium free phosphor coating [36]. The spots on the fluorescent screen can be seen by eye, but a camera is mounted at the viewport to collect an image for computer analysis. The LEED apparatus mounted on the HPXPS instrument is a ErLEED system built by SPECS GmbH [36].
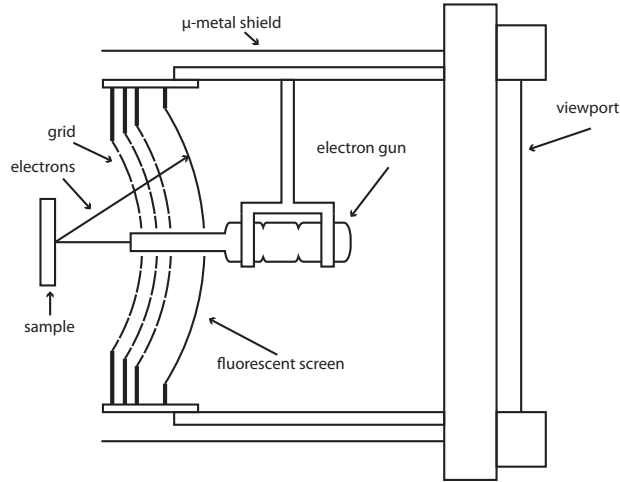
Fig. 2.4: A schematic drawing of the LEED apparatus. Image adopted from [36].

2D diffraction and reciprocal vectors

A convenient way to find the real space structures from LEED diffraction patterns is by the use of wave vectors. The magnitude of the wave vector for the incoming electrons is given by

$$|\mathbf{k}_0| = \frac{2\pi}{\lambda}, \tag{2.12}$$

where λ is the de Broglie wavelength of the electrons. Constructive interference from a 1D surface lattice is given by Bragg's law:

$$n\lambda = a \cdot \sin\theta_a, \tag{2.13}$$

where a is the lattice constant, θ_n is the scattering angle, and n is the order of scattering. Combining Eq.(2.12) and Eq.(2.13) yields

$$|\mathbf{k}_0| \sin\theta_a = \left(\frac{2\pi}{a}\right) n, \tag{2.14}$$

where $|\mathbf{k}_0| \sin\theta_a$ is the momentum component parallel to the surface of the incident electron $\mathbf{k}_{\parallel}$. Furthermore, the above formula states that the momentum exchange between the surface lattice and electron is quantised in steps of $2\pi/a$. In a LEED experiment, the initial electrons are coming in perpendicular to the surface and no $\mathbf{k}_{\parallel}$ exists. In order for the electrons to change direction, they must exchange momentum with the surface lattice for momentum conservation, which yields discrete beams as momentum can be exchanged in quantised steps only.

If a periodicity of the first surface lattice is introduced in another direction, the diffraction will be determined by

$$|\mathbf{k}_0| \sin \theta_b = \left(\frac{2\pi}{b}\right) m, \tag{2.15}$$

where b is the lattice constant in the new direction. This imposes a restriction to the diffraction which is only allowed when both Eq.(2.14) and Eq.(2.15) are satisfied. The exchange of parallel momentum is thus restricted to a two dimensional lattice vector, $\mathbf{G}$, given by

$$\mathbf{G} = \Delta \mathbf{k}_{\parallel} = n\frac{2\pi}{a} + m\frac{2\pi}{b}, \tag{2.16}$$

where $\Delta \mathbf{k}_{\parallel}$ is the change in parallel momentum of the impinging electrons. The reciprocal space lattice created by a surface upon diffraction can be constructed by applying that the momentum transfer vector is a linear combination of reciprocal lattice vectors:

$$G = n\mathbf{a}^* + m\mathbf{b}^*, \tag{2.17}$$

$$|\mathbf{a}^*| = \frac{2\pi}{|\mathbf{a}|}; \ |\mathbf{b}^*| = \frac{2\pi}{|\mathbf{b}|}; \ \mathbf{a}\mathbf{b}^* = \mathbf{a}^*\mathbf{b} = 0, \tag{2.18}$$

where $\mathbf{a}$ and $\mathbf{b}$ are real space vectors and $\mathbf{a}^*$ and $\mathbf{b}^*$ are their respective reciprocal space counterpart.

3. The HPXPS Instrument

The need to bridge the pressure gap is evident and much instrumentation has been developed to address this issue. At other synchrotron facilities, e.g. BESSY and the ALS, there exist HPXPS instruments which address the pressure gap. When using the instrument, the entire analysis chamber is filled with gas [18]. A small aperture nozzle fixed on the analyser separates the high pressure (HP) environment in the analysis chamber from the vacuum in the analyser. This makes for fairly easy HP experiments. However, by filling the entire analysis chamber with mbar pressures of gas, long pumping times and often bake-out is required to regain UHV conditions as the gas molecules "stick" to the chamber walls. UHV conditions are widely employed and much knowledge has been gained during UHV studies. Therefore, UHV measurements are desired to link HPXPS studies to previous UHV results.

At the instrument at MAX-lab the HP environment is confined to a small cell inside the analysis chamber to enable for HP measurements, an idea which was developed here in Lund. Actually, a small volume is suitable for reaction measurements as small product gas volumes is easier to detect. The cell itself is mounted onto a manipulator which enables it to be attached to the prelens of the analyser, which enables two modes for UHV and a HP measurements, as depicted in Figure 3.1. In UHV mode [Figure 3.1(a)],
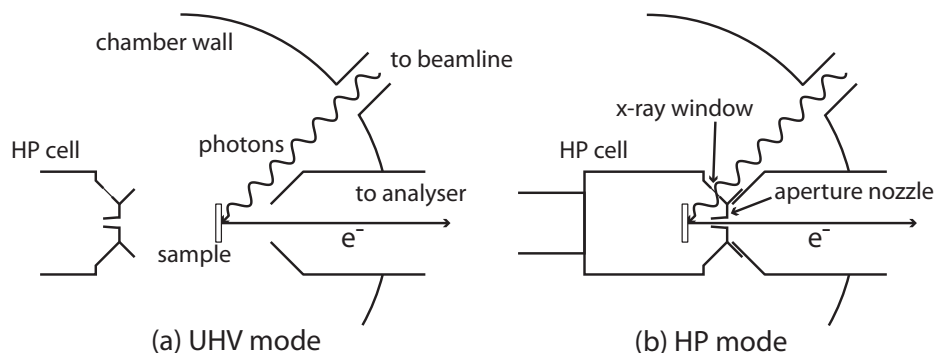

Fig. 3.1: Schematic view of the two operation modes.

the sample is held by another manipulator (not shown in the figure) which is mounted vertically on the instrument. The photons enter the analysis chamber through a flange, which connects the instrument and the beamline. The beamline is connected to the MAX II electron storage ring and serves to focus and monochromatise the photon beam. The beamline will be described in greater detail in section 3.2. The UHV mode is used mainly to probe the sample in a clean environment, which is important for *ex situ* characterisation and comparison with previous studies.

In HP mode the cell is attached to the prelens of the analyser and the sample is subsequently transferred using a wobble stick [Figure 3.1(b)]. The HP cell is equipped with an x-ray window, allowing the photons to enter. An aperture nozzle mounted on the cell allows for high pressures in the cell while keeping the vacuum in the rest of the system. After the HP experiment, the cell can be pumped down quickly and the sample can again be transferred onto the UHV manipulator for further UHV characterisation or sample treatment.

3.1   Vacuum system layout

An important part of my work has been to install and test the HPXPS instrument at beamline I511 at the MAX II electron storage ring; therefore I will describe its special features in detail. In Figure 3.2 a schematic view of the vacuum system of the instrument is shown. The system consist of two main vacuum chambers, a load lock for easy sample in-transfer, a load lock for the HP cell, and the electron energy analyser. The sample is transferred to the different parts of the system with the help of a transfer arm, the UHV manipulator, and a wobblestick. The load lock is used to transfer samples into the system from the outside without breaking the vacuum of the main chambers. The preparation chamber is mounted on top of the analysis chamber, and a vertically mounted UHV manipulator is used for transfer between the chambers. The HP cell is mounted on a horizontal manipulator which is used for transfer of the cell from the HP load lock into the analysis chamber. The HP cell is attached to the analyser aperture prior to gas injection and a wobblestick that enables transfer of samples from the UHV manipulator into the HP cell. The system is also equipped with a gas panel allowing for mixing of up to three gases to be entered in the HP cell or to dose the individual gases to a sample in the preparation chamber. All chambers are pumped by turbomolecular pumps, which in turn are pumped by dry scroll pumps. In addition, the preparation and analysis chamber are
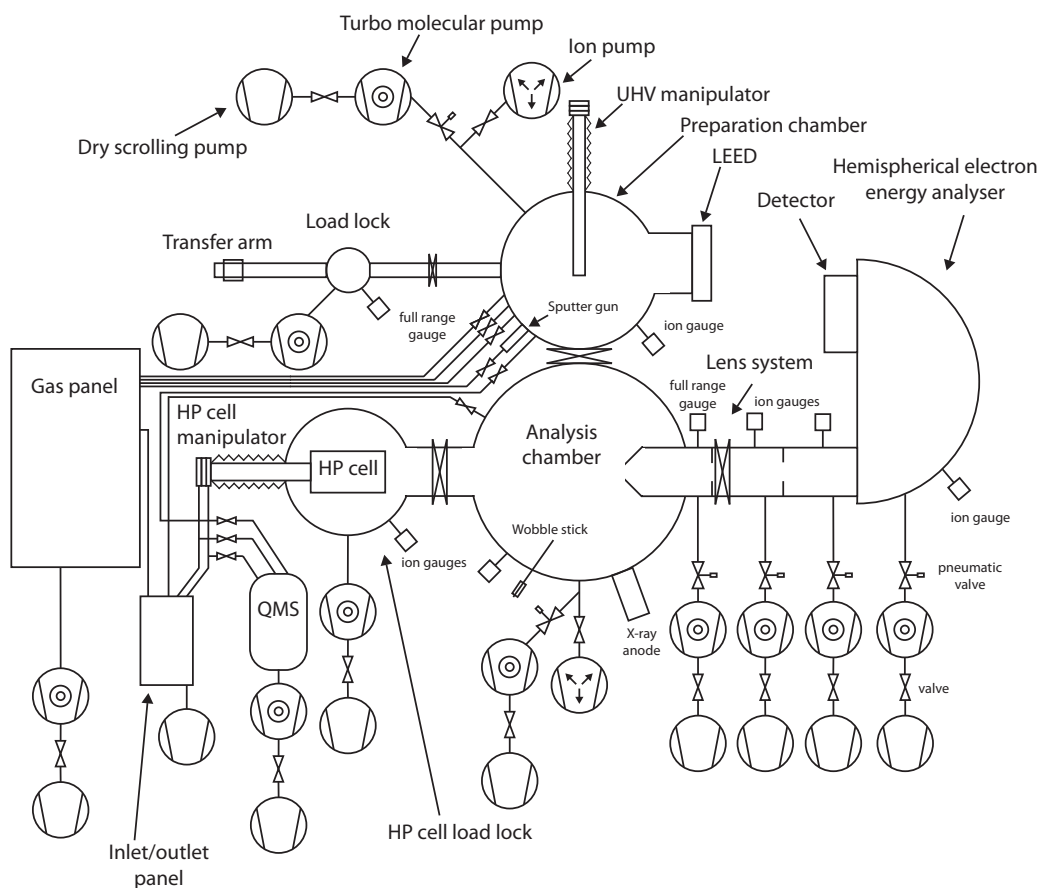
Fig. 3.2: A schematic image of the vacuum chambers, transfer system and pumps.

equipped with ion and titanium sublimation pumps in order to reach UHV conditions as fast as possible. The different components attached on the chambers as well as the beamline will be described in greater detail in the following sections.

3.2   Beamline I511 at the MAX II electron storage ring

The HPXPS endstation is, as mentioned before, positioned at beamline I511 at the MAX II electron storage ring. Beamline I511 is a soft X-ray beamline equipped with a modified SX-700 monochromator for high photon energy resolution [37], similar to the ones used by beamlines I411 [38] and I311 [39].

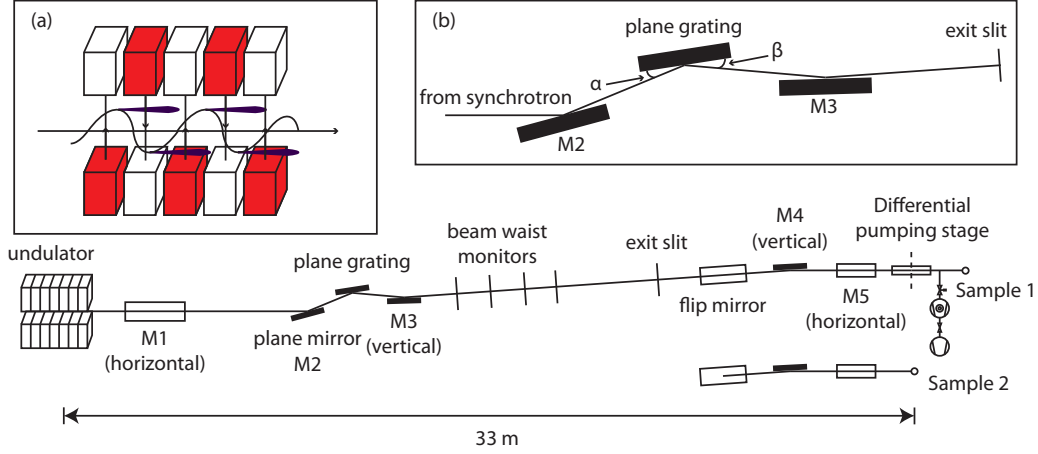A schematic image of the beamline can be seen in Figure 3.3.

Fig. 3.3: A Schematic drawing of the I511 beamline. Image adopted and modified from Ref. [37]. Inset (a) shows the working principle of an undulator, where the red and white blocks represents magnetic north and south poles, respectively. Inset (b) shows an enlarged view of the monochromator optics.

The Undulator

I511 is an undulator beamline. An undulator is a device which has arrays of magnets to create an alternating magnetic field in the path of the electrons in the storage ring (cf. inset (a) in Figure 3.3). The undulator at beamline I511 has two magnetic arrays arranged vertically and in total 49 periods, each of 52 mm length. The electrons travel inside the gap between the upper and lower magnet array. Each of the magnetic periods acts as a bending magnet [22]. Whenever the electron trajectory is bent radiation is produced. The total yield will thus be enhanced by a factor N compared to a single bending magnet, where N is the number of dipoles. Additionally, the radiation will interfere at the many co-linear points, as the length between successive bends are multiples of the wanted wavelength, producing quasi-monochromatic peaks [40] given by the undulator equation

$$\lambda_n = \frac{\lambda_u}{2n\gamma^2}\left[1 + \frac{K^2}{2} + \gamma^2\theta^2\right] \quad n = 1, 2, 3, 4, ... \tag{3.1}$$

Here λ_u is the period length, $\gamma = E_e/m_0c^2$, θ is the observation angle relative to the average electron direction, n is the harmonic number and $K = 0.934\, B_0[\mathrm{T}]\lambda_u[\mathrm{cm}]$ where B_0 is the peak magnetic field. If the magnetic

field is sinusoidal, $K = \gamma\delta$ where 2δ is the full angular excursion of the electron beam. The factor K is used to differ between the so-called wigglers and undulators, with $K > 1$ and $K < 1$, respectively.

The undulator at beamline I511 was manufactured by VTT. The undulator gap, i.e. the gap between the upper and lower array of magnets, can be varied from 17 mm up to 250 mm yielding usable photons energies from 50 eV up to about 1500 eV with a calculated maximum brilliance of $5 \cdot 10^{17}$ photons/s/100 mA/0.1% BW/mm^2/mrad^2 [37]. The photon intensity varies with photon energy. A graph showing measured intensity as a function of photon energy is presented in Figure 3.4.
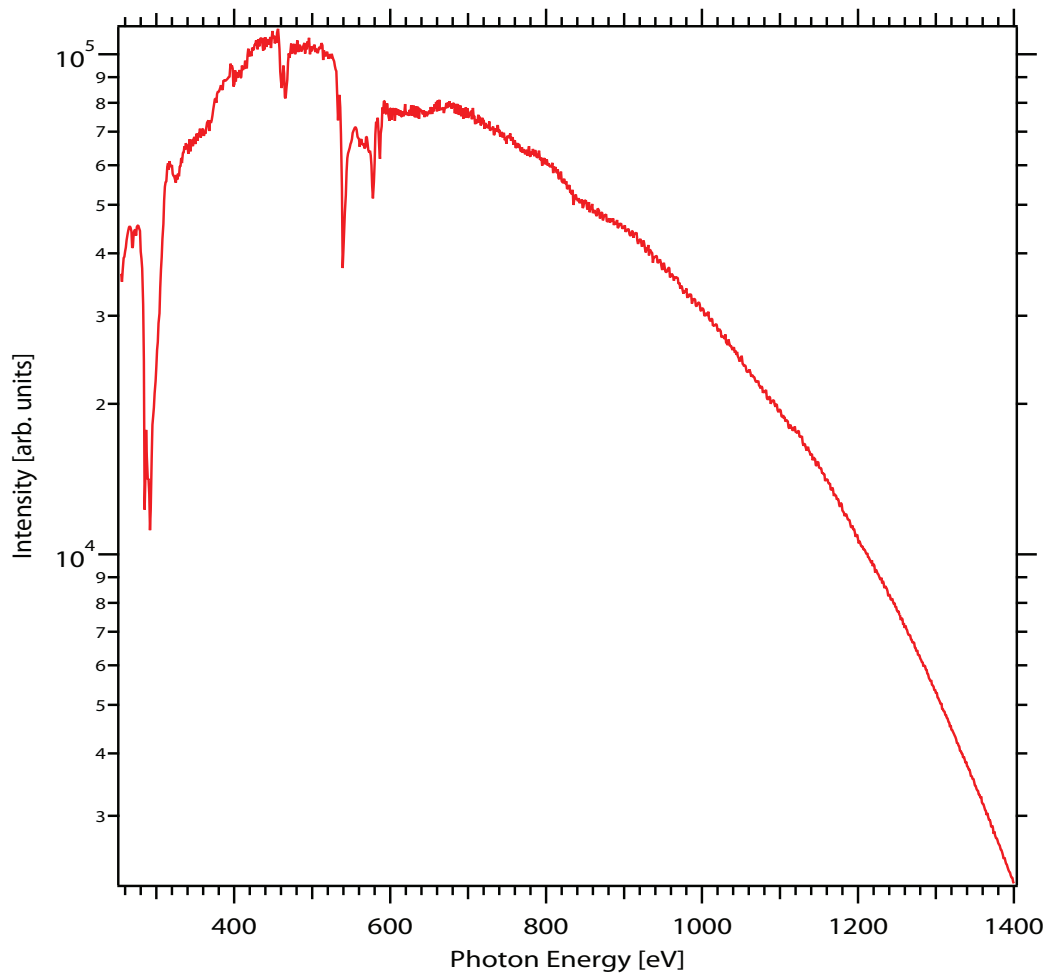

Fig. 3.4: A graph showing the photon intensity as a function of the photon energy for photon energies relevant during HP experiments

Beamline optics

The monochromator is a plane grating monochromator (PGM) of SX-700 type, originally manufactured by Carl Zeiss. It consists of a plane mirror, plane grating, a vertical mirror, and an exit slit (cf. inset (b) in Figure 3.3). The plane mirror (M2) focuses the light onto the plane grating and the dispersed light then impinges on a spherical focusing mirror (M3) which focuses the light onto the exit slit. The slit can be adjusted continuously from 0 μm to 800 μm. The monochromator deflects the light by 4° with respect to the plane of the incoming light. The photon energy is selected by rotating the plane mirror and grating to satisfy the focusing condition $\sin \beta / \sin \alpha$=const where α and β are the grazing angles at the grating [41]. A Au coated grating with 1221 l/mm is normally used for delivering photons with a high light resolution over a broad spectral range, but a Ni coated grating with 250 l/mm is also available [37]. In UHV typically a slit of 20-50 μm is used giving a light resolution of 20-80 meV. However, the resolution depends strongly on the photon energy which needs to be considered when choosing slit settings. For HP measurements a slit size of 100 μm is typically used. This lowers the resolution but the increased intensity is needed.

Behind the monochromator exit slit, a flip mirror is mounted on the beamline allowing for the use of two branch lines one of which is the HPXPS branch line. The light is then refocused by a vertical and a horizontal spherical mirror, M4 and M5 in Figure 3.3. This refocusing system was built for another instrument which the HPXPS instrument replaces. As a result, the HPXPS instrument is positioned behind the focus, which yields a large spot size, 2x3 mm^2, which unfortunately limits the performance of the setup. The beamline will be exchanged as part of the SPECIES project in 2013, which will resolve the spot size issue.

Differential pumping of the beamline

During HP experiments the beamline needs to be protected from the HP environment in order to avoid contamination of the mirrors. Therefore, a differential pumping stage has been installed in between the refocusing mirrors and the instrument. The differential pumping stage has pneumatic valves on each side and consists of an ion pump and a turbo pump. The ion pump is mounted for line of sight pumping, similar to the differential pumping at beamline I3 of the MAX III electron storage ring [42]. On the instrument side of the pump, two valves are found, one for closing between the beam-

line and the instrument, and one fast closing valve for security. A gauge at the refocusing mirrors continuously monitors the pressure; if it rises, the fast closing valve will close. A sudden rise in pressure typically implies that the x-ray window in the cell has broken (see section 3.4). When the window breaks, a jet of molecules is emitted from the high pressure environment into the vacuum of the beamline, meaning that the valve must be closed in order to preserve the vacuum and avoid contamination of the refocusing mirrors. Also, as the valve cannot react fast enough, the ion and turbo pump will ensure that the initial gas jet does not destroy the vacuum.

As mentioned previously, the refocusing on the beamline was built for another system. The previous system did not have a differential pumping stage, and the old system was therefore positioned much closer to the refocusing optics. With the differential pumping stage installed, the new HPXPS system is positioned further away from the refocusing optics and the sample is therefore placed behind the focus point of the light.

3.3 The Hemispherical Electron Energy Analyser

The spectrometer of the HPXPS instrument is a PHOIBOS NAP 150 hemispherical electron energy analyser built by SPECS GmbH. A schematic image of the analyser is shown in Figure 3.5. The spectrometer consists of four separated pumping stages in order to keep the detector below a limit of $5 \cdot 10^{-8}$ mbar when the sample is exposed to gases in the mbar regime. During HP experiments, the HP cell is attached to the spectrometer. The nozzle in front of the HP cell allows electrons to reach the analyser and a small amount of gas to flow through the small opening into the prelens. The present setup has a nozzle with a one mm opening, but nozzles with other diameters can be mounted readily. A turbo pump with a pumping speed of 500 l/min is mounted on the prelens pumping state. This turbo pump reduces the pressure by four orders of magnitude as compared to the pressure in the HP cell, when a 0.3 mm aperture is installed. The prelens is equipped with a deflector for adjustment of the analyser focus and electrostatic lenses to focus the electrons onto a two mm aperture that separates the prelens from the rest of the lens system. Directly behind the aperture a UHV valve is positioned allowing a complete seal between the prelens and the rest of the spectrometer. The second pumping stage contains the first of the two lens elements. These lens elements focus the electrons onto the entrance slit of the analyser and decel-
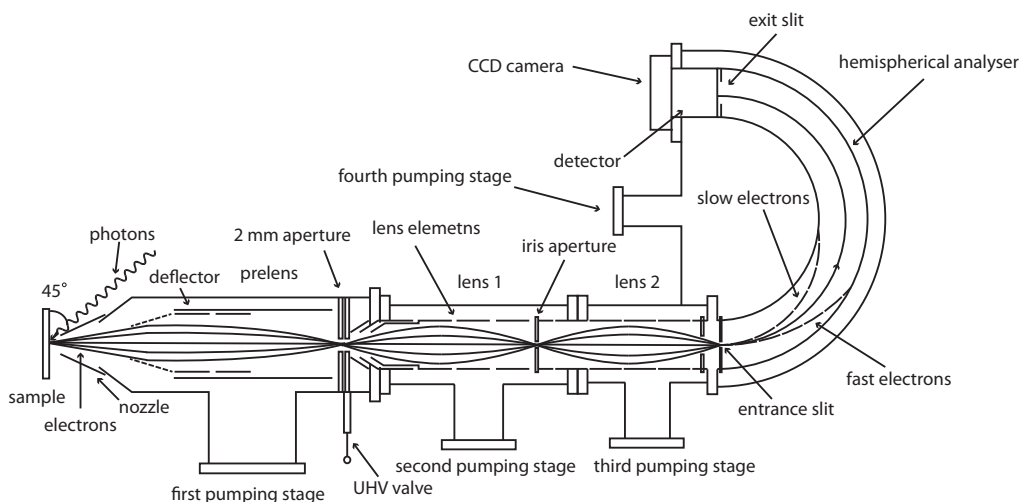
Fig. 3.5: A schematic view of the PHOIBOS NAP 150 hemispherical electron energy analyser.

erate/accelerate the electrons so their kinetic energy match the pass energy of the hemisphere. The first lens focuses the electrons onto an iris aperture. The iris aperture separates the two lenses and the second and third pumping stage. By selecting a small iris aperture, a higher pressure difference between the pumping stages can be achieved and thus a higher pressure in the HP cell, at the cost of electron intensity. Lens 2, which is contained in the third pumping stage, focuses the transmitted electrons onto the entrance slit of the hemispherical analyser. The fourth pumping stage contains the hemispherical analyser and detector. The electrons which pass through the entrance slit will feel the field between the hemispheres and their trajectories will change. If the kinetic energy corresponds to the pass energy, the electrons will pass through to the detector. If the kinetic energy of the electrons deviates from the pass energy too much, they will hit either the inner or outer hemisphere. The detector consists of a multi-channel plate (MCP), where the impinging electrons will be multiplied before they hit a fluorescent screen. A CCD camera mounted from the outside images the fluorescent screen and detects the electrons as they hit the screen. The CCD has 640x480 pixels and the usable area is 38.7x20 mm^2, which is the area of the MCP.

As the electrons need to travel quite a long distance to reach the detector, the spectrometer needs to be shielded from **B**-fields as they would have a considerable impact on the trajectories of low energy electrons. The whole inner part of the spectrometer is encased in two layers of 1.5 mm thick μ-metal to screen external magnetic fields, the Earth's **B**-field included. All parts inside the encasing are made of non-magnetic materials. In addition,

the analyser is equipped with a trim coil around the outer hemisphere. This trim coil is used to adjust the total magnetic field inside the hemisphere so it is equal to zero.

The electrons passing the hemispheres travel along an ideal path with radius R_0 with a small deviation. This uncertainty gives the resolution of the analyser, which is given by

$$\Delta E_a = \left(\frac{S}{2R_0} + \frac{\alpha^2}{4} \right) E_{pass},$$ (3.2)

where S depends on the entrance- and exit slits and thus is a constant of the analyser, α is half the acceptance angle of the emitted electrons, and E_{pass} is the hemisphere pass energy. The resolution is determined by the CCD as it records ΔE and divides it into a number of channels. The pass energy is different depending on which analyser mode is chosen [43]. The PHOIBOS 150 NAP analyser has two operation modes, Fixed Retarding Ratio (FRR) and Fixed Analyser Transmission (FAT). In FRR mode, the pass energy is given by

$$E_{pass} = \frac{E_{kin} - \Phi}{R},$$ (3.3)

where E_{pass} is the pass energy of the hemisphere, E_{kin} the kinetic energy of the impinging electrons using the Fermi energy as reference, Φ the work function of the detector, and R is the retardation ratio which is kept constant. FRR mode is typically used for Auger spectra as the resolution increases at high kinetic energies, allowing the detection of high energy peaks, while suppressing the strong, low energy background. The pass energy for FAT-mode is given by

$$E_{pass} = -ek\Delta V,$$ (3.4)

where e is the electron charge, ΔV is the potential between the hemispheres, and k is a calibration constant given by the radii of the hemispheres; for this analyser $k = 0.9375$ [43]. The FAT mode is used most commonly as the resolution does not depend on the initial kinetic energy of the photoelectron.

The transmitted intensity is proportional to the acceptance angle and sample area as well as the ratio between the pass energy and the kinetic energy of the electrons [43], thus

$$I \sim \Delta E_a \Omega_0 A_0 \frac{E_{pass}}{E_{kin}} \sim \frac{E_{pass}^2}{E_{kin}},$$ (3.5)

where Ω_0 is the acceptance angle of the analyser, A_0 is the sample area and thus analyser constants.

The analyser has eight different entrance slits and three different exit slits. These slits have different sizes, which result in different resolutions. However, only one of the exit slits is normally used together with one of the 5 rectangular entrance slits and usually a 1 x 20 mm and a 3 x 20 mm slit are used for UHV and HP measurements, respectively. In Table 3.1 the entrance slit sizes available as well as the analyser resolution obtained with the slit for different pass energies is shown.

Tab. 3.1: The different analyser resolutions obtained for the most commonly used slits and pass energy combinations. All values are given in eV unless specified.

Slit size [mm]	$E_p = 10$	$E_p = 20$	$E_p = 30$	$E_p = 50$	$E_p = 100$
0.2 x 20	0.083	0.17	0.25	0.41	0.83
0.5 x 20	0.093	0.19	0.29	0.46	0.93
1 x 20	0.11	0.22	0.33	0.55	1.10
3 x 20	0.18	0.35	0.53	0.88	1.76
7 x 20	0.31	0.62	0.93	1.55	3.10

3.4   The high pressure cell

In order for a HPXPS experiment to be conducted, a HP sample environment separated from the analyser by a small aperture is required. Ogletree et al. [16, 18] used an aperture fixed to the analyser nozzle and thus between the analyser and analysis chamber. This is an easy-to-use method, but if the analysis chamber is filled with a near ambient atmosphere it will require bake-out before UHV conditions are reached again. This is troublesome as UHV characterisation of samples is important, partly due to the possibility of higher resolution but most importantly, it provides a link to standard UHV experiments. Also, if the instrument is placed at a synchrotron beamline pumping time should be held short as beamtime is limited.

The idea developed in Lund is to use a retractable and exchangeable HP cell, as depicted schematically in Figure 3.6. It is mounted on a manipulator, and the cell itself holds the aperture nozzle required for differential pumping during HPXPS experiments. The cell can be attached to the prelens nozzle using a bayonet locking mechanism, and a rubber gasket ensures that the analysis chamber is kept in vacuum during the experiment. After an experiment, the cell may be pumped down quickly and withdrawn, allowing UHV experiments within 10 minutes. The ability to exchange cell allows users to design their own cells, making the instrument capable of a wide range of investigations.
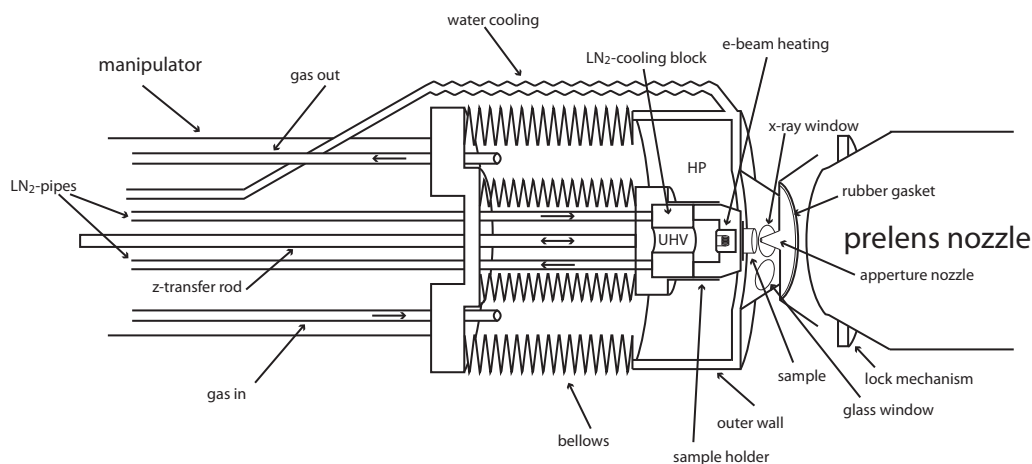
Fig. 3.6: A schematic drawing of the HP cell near the prelens nozzle.

As seen in Figure 3.6, the HP cell consists of two bellows, one holding the outer wall while the other houses the sample holder. While detached, the whole cell is moved by the manipulator. When the cell is attached to the prelens the outer bellow is fixed and movement of the sample inside the cell is possible. This is an important feature as delicate samples suffers from beam damage and probing different parts of the sample is thus desired. However, with the present size of the beam nearly the whole sample is illuminated.

The inner bellow interior is kept in UHV to enable the use of an e-beam heating system. UHV is required as near ambient atmospheres of, e.g O_2, would break the filament in the heater. The e-beam heater used in this cell enables temperatures up to 500° C, and the LN_2 Dewar cools the sample to -60° C. As the heating and cooling parts are separated from the high pressure environment, cooling/heating of the sample in near ambient pressures is possible without interference from catalytic activity on the active components. The outer walls are continuously cooled with water so that only the sample and sample house are heated, which ensures that no reaction takes place at the cell walls.

The light enters through an x-ray window in the cell wall near the aperture. In total the cell has four windows, two soft x-rays windows for two different light sources, one being the synchrotron and the other a fixed x-ray source. The x-ray windows are composed of a 200 nm Si_3N_4 membrane coated with a 100 nm Al film. The x-ray transmission through the window is shown in Figure 3.7. The other two windows are made of glass for lighting and camera view. The camera view is important as 100 μm precision is needed when positioning the sample.
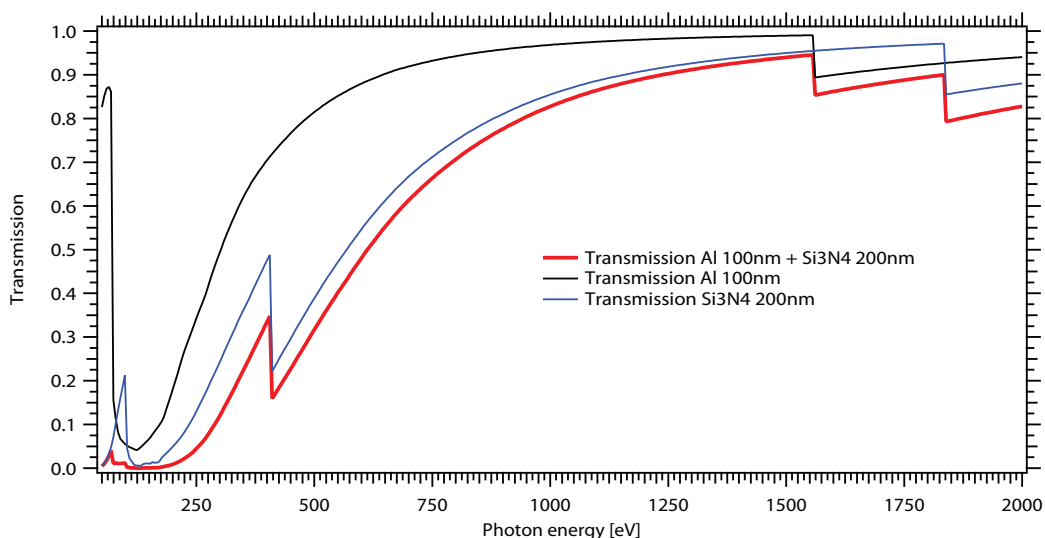
Fig. 3.7: The transmission trough the different membranes and the x-ray windows as a function of photon energy. Data is based on [44] and the image is adopted from [45]

Access to the sample seat is made possible by a door, which can be opened by a wobblestick in the analysis chamber after docking to the prelens, cf. Figure 3.8 (a) and (b). In panel (a) the cell is approached bot not docked, while in panel (b) the cell is docked and the door is opened. Additionally, in panel (b) a sample is positioned in the wobblestick and about to be loaded into the HP cell. Before an experiment, the z-transfer rod extends the sample holder and the sample approaches the aperture nozzle.

In Figure 3.8 (c) and (d) two images from samples approached to the aperture nozzle is shown. In panel (c) is an image of a fluorescent sample, the large light spot is clearly visible. Panel (d) shows an Ir(111) crystal approached to the aperture nozzle. The sample-aperture distance is approximated by looking at the nozzle to mirror-image distance.

Sample Position

When positioning the sample in front of the aperture, the aperture-sample distance needs to be considered. Ogletree et al. [16] investigated the molecular flow through an aperture orifice from an ideal gas theory point of view. They found that if an aperture of radius R separates the high pressure region, pressure P_0, from a vacuum region, the pressure felt by an electron travelling along a central axis can be expressed as
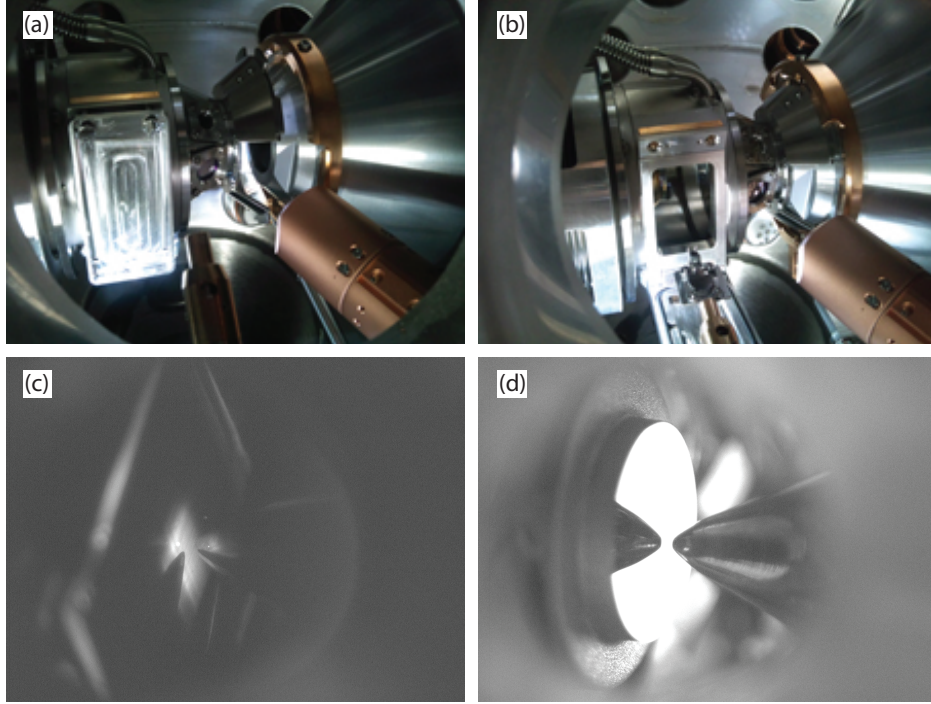
Fig. 3.8: Pictures of the HP cell. (a) The cell before it is docked. (b) The docked cell and the sample is to be loaded through the open door. (c) a fluorescent sample inside the cell. (d) an Ir(111) crystal approached to the aperture nozzle.

$$P(z) = P_0 \frac{1}{2}\left(1 - \frac{z}{\sqrt{1+z^2}}\right), \qquad (3.6)$$

where z is the electron distance from the aperture measured in units of R, cf. Figure 3.9(a). In the figure the pressure is calculated along the dashed line. The plot in Figure 3.9(b) shows how the ratio between $P(z)$ and P_0 varies with z. Further, it is seen that the pressure felt by the electron is significantly lower than P_0 close to the aperture opening, but it quickly rises as the the distance to the aperture increases. Also, the pressure at the vacuum side of the orifice drops quickly. If the sample is placed at $-2R$, the pressure is about 95% of P_0 while at $-1R$ the pressure is 85% of P_0. Following the above reasoning, an appropriate sample-aperture distance is at least $2R$. Actually, experience shows that the distance should be slightly larger, namely two times the aperture diameter [46]. Therefore, appropriate sample-aperture distances are 2 mm and 0.6 mm, for the 1 mm and 0.3 mm apertures, respectively.

The pressure in the HP cell is measured on the gas outlet line. With the present gauge, this works for pressures above 0.1 mbar. At lower pressures,
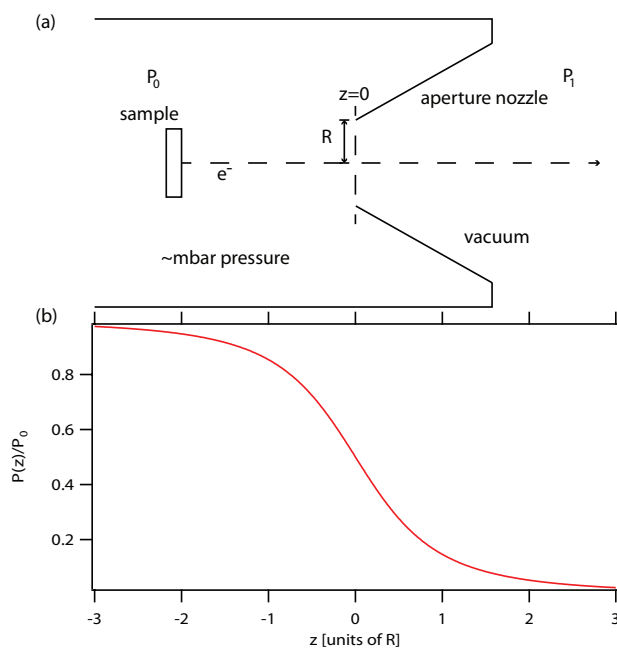
Fig. 3.9: Pressure in the HP cell. (a) Geometry. (b) The ratio between $P(z)$ and P_0 along the dashed line.

the pressure in the prelens can be used to determine the pressure in the cell. The gauge in the prelens is a combined pirani and ion gauge, which respond different to different gases. Additionally, the pumping speed trough the orifice is gas dependent. In Figure 3.10 the pressure characteristics for different gases in the gas line and prelens are presented. The gauge on the gas line shows a linear relation independent of what gas is used [panel (a)]. The pressure in the prelens is gas dependent and therefore the gas type needs to be considered when calibrating pressure [panel (b)]. The graphs (cf. Figure 3.10) demonstrate the ability of the HPXPS instrument to perform controlled measurements in the whole UHV to near-ambient range.

3.5 Alignment

As for any instrument using light alignment was required before the instrument could be brought into operation. The monochromator deflects the light upwards by 4 °, and therefore the instrument is mounted on a triangular-shaped supportat a height of 1.2 m above the floor. The triangle is supported by three pillars with a z-adjustment block at each corner of the triangle, and the instrument is built on a $x - y$ table, which enables adjustments in both
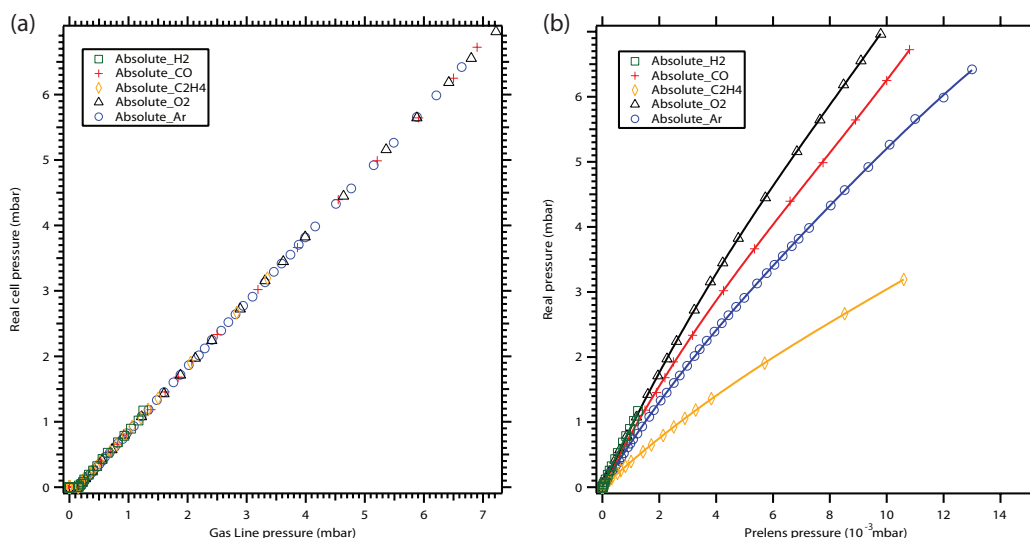
Fig. 3.10: Relationship between real cell pressure, gas line pressure and prelens pressure. (a) Plot of the real cell pressure as a function of gas line pressure. (b) Real cell pressure as a function of prelens pressure.

the vertical and horizontal planes.

When aligning an instrument to a synchrotron beamline, a number of things need to be considered, the most fundamental being that the position of the light and analyser focus must overlap. The light position may be moved by adjusting the refocusing mirrors. The focus of the detector can also be moved by adjusting the deflector settings. The range of these primary adjustments is limited but give a certain amount of flexibility. However, since this is a setup for high pressure experiments, additional considerations are introduced:

- The differential pumping stage towards the beamline severely restricts adjustments of light position as it holds apertures in both ends.

- The analyser focus is fixed by the small size of the HP cell aperture nozzle.

- The angle between light and analyser must be nearly perfect as it shall pass through a window.

In order to align the setup, the whole instrument needs to be moved as the fixed analyser focus needs to overlap with the fixed light position.

To align the instrument a two-fold alignment procedure was used. A fluorescent sample made the light visible for the eye and was used to position the light. As the fluorescent sample is insulating and XP spectra cannot be

recorded on it, a Ag(111) crystal was used to align the focus of the analyser with the emitted photoelectrons. Initial alignment of the instrument was carried out in the UHV manipulator using the fluorescent sample. The light was positioned at an approximate position in front of the prelens nozzle by moving the entire instrument using the $x - y$ table. The Ag(111) crystal was loaded for initial alignment of the analyser by recording XP spectra and changing the deflector settings to change the focal point and maximising count rates. After the initial alignment, the fluorescent sample was loaded into the HP cell, which was attached to the prelens nozzle. The light position was again moved to an approximate position in front of the small aperture. When an approximate position of the light was found, the Ag(111) crystal was loaded into the HP cell for final alignment. Here, the lens settings of the analyser were adjusted to obtain maximum electron count rates. This was done by exciting the Ag 3d core level while slightly adjusting the lens settings and simultaneously monitoring the electron count rate. For final alignment, the light position was adjusted while the electron count rate from the Ag(111) crystal was monitored. When maximum electron count rates was achieved, the procedure was repeated in order to find a better position. When no increase in count rate could be found, the instrument was considered to be aligned.

3.6   The X-ray Anode

As the instrument is mounted on a branched beamline, the amount of synchrotron light is limited and light is available only 50% of the time. In order to dedicate the synchrotron light to experiments, the HPXPS instrument is equipped with an x-ray anode to be used for sample preparation when the synchrotron light is unavailable.

The x-ray anode is a XR-50 built by SPECS GmbH. The x-ray anode is equipped with two heads, one made of Al and the other made of Mg as depicted in Figure 3.11. The radiation is produced by bombarding one of the metal targets with high energy electrons. This leads to core ionisation of the metal. The ionised atom can then replenish the core hole from a higher orbital, thus emitting characteristic x-rays at 1486.6 eV (Al K$_\alpha$) and 1253.6 eV (Mg K$_\alpha$) for Al and Mg, respectively [47]. Additionally, the electron bombardment will produce bremsstrahlung, forming a continuous spectrum.
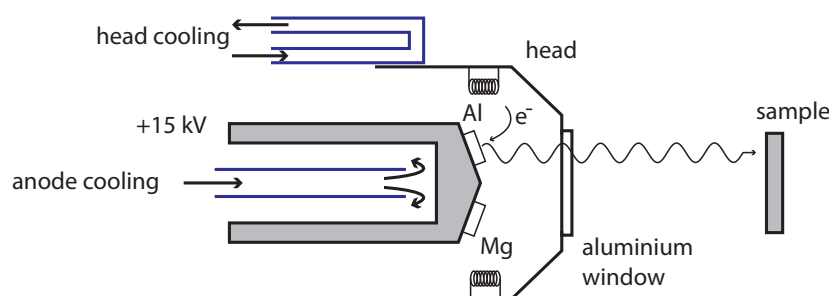
Fig. 3.11: Schematic drawing of the XR-50 x-ray anode head. Image adopted from Ref. [47].

The aluminium window at the x-ray anode head suppresses the bremsstrahlung, making the radiation more monochromatic. Also, it stops electrons emitted from the filaments from reaching the analyser.

3.7   Gas system

The HPXPS instrument is equipped with the gas panel schematically depicted in Figure 3.12. At present, there are four gases available and there is room for adding two more. The available gase lines are for Ar, O_2, CO and a gas line dedicated to hydrocarbons. Ar is mainly used for Ar-sputtering in the preparation chamber, while the three other are used for high pressure experiments or vacuum preparations. In order to obtain very high purity of the gases, each gas line, except for Ar, is equipped with a gas purifier. The gas purifiers consists of porous materials through which gas is flown. The material will bind any contaminants, such as H_2O. The gas purifiers used on the gas panel are commercial Gaskleen II Gas Purifiers produced by PALL [48]. To further improve purity in the CO and the hydrocarbon gas line, they are equipped with cooling coils to freeze out impurities as the purity is especially important in HP mode. For example, when one buys ultra-clean CO one gets purity grade N48 (99.998 % CO). The sample is therefore exposed to 0.002% "contamination". In UHV this relatively small amount is neglected. However, using the ideal gas law, $pV = nRT$, it is clear that by increasing the pressure by a factor of 10^{10} the contamination cannot be neglected, since it well might be in the ppm range.

After the gas purifier, the gas lines are divided; the lines marked "out" in Figure 3.12 refer to gas lines going to the preparation chamber. The lines going to the HP cell line are controlled by mass flow controllers. The flow controllers are GF125 Analog I/O controllers manufactured by Brooks Instru-

ments. These mass flow controllers measure the heat loss in a small, heated channel. The heat loss is related to the flow of gas and used by a feedback loop to control a valve which sets the gas flow [49]. The heat transfer is strongly gas dependent and each controller needs to be calibrated for the intended gas. The flow controllers used are so-called multi-flow controllers, meaning that they support multiple gases and can be re-calibrated for each gas. Additionally, the GF125 controllers are fitted with pressure transducers [50]. The pressure transducers feel changes of gas pressure in the gas line and corrects for the change in the flow measurement. The flow controllers are controlled with a computer, making flow control during experiment easy.
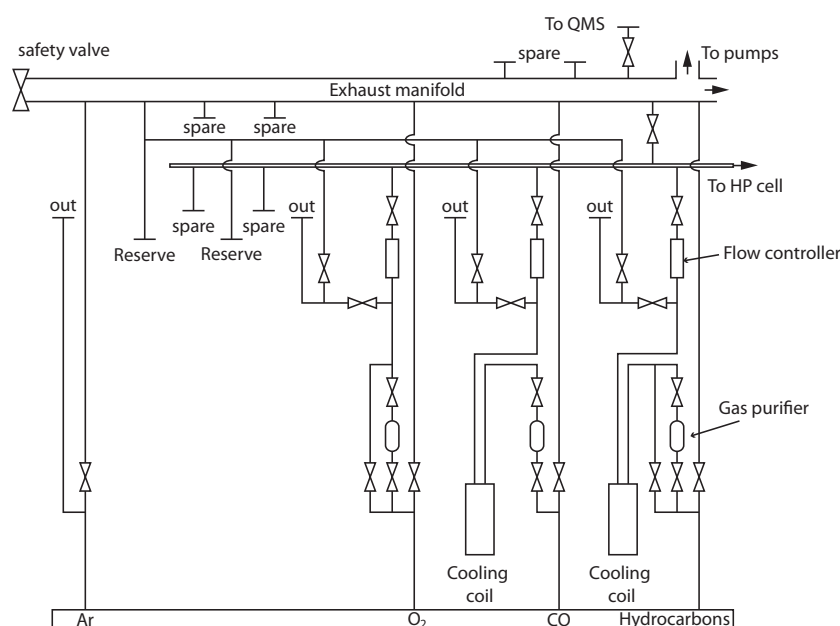

Fig. 3.12: Schematic image of the gas panel. Image adopted from [49].

3.8 Reactivity Measurements

While performing high pressure experiments, it can be useful to see the reaction products. XPS can detect these reaction products in either the gas phase or adsorbed on surfaces. However, XP spectra can be time consuming to acquire and the start of reaction can thus be missed. Therefore, it is useful to have a quadrupole mass spectrometer (QMS) available for gas phase reaction product detection. The HPXPS instrument is equipped with a QMS, which is mounted on a small chamber attached close to the gas outlet of the

HP cell. By flowing the gas through the cell, the gas outlet will be filled by both the reactive species as well as the reaction products.

A QMS consists of three major parts, an ionizer, a mass filter and a detector [51] as illustrated in Figure 3.13. In the ionizer, two filaments emit electrons which are accelerated towards a source grid. Gas molecules are hit by these electrons which ionize them, leaving them positively charged. The positive ions are accelerated towards the mass filter by a negatively charged focus plate as well as a lens. The mass filter consists of four rods forming a quadrupole. The **E**-field in the quadrupole consists of two components, a DC- and a RF component. The RF component quickly varies the field, which forces the ions to take an oscillating path. The force on the ions depends on their charge-to-mass ratio, meaning that it is possible to select ions by making the RF-oscillations such as only one charge-to-mass ratio is in resonance with the filter. The ions which are not in resonance hit the rods, and thus the ions supposed to reach the detector can be selected by sweeping the frequency of the RF field. The QMS at the HPXPS instrument is a Dycor LC-D Residual Gas Analyzer built by AMTEK [51] which houses a Faraday cup detector equipped with an electron multiplier. The incoming ions hit a charged plate in the electron multiplier and start an electron avalanche that amplifies the signal. The electron cascade emitted by the multiplier then reaches the Faraday cup that becomes charged. The Faraday cup is connected to ground and by measuring the ground current resulting from the charging, the signal from the ions reaching the multiplier is extracted.
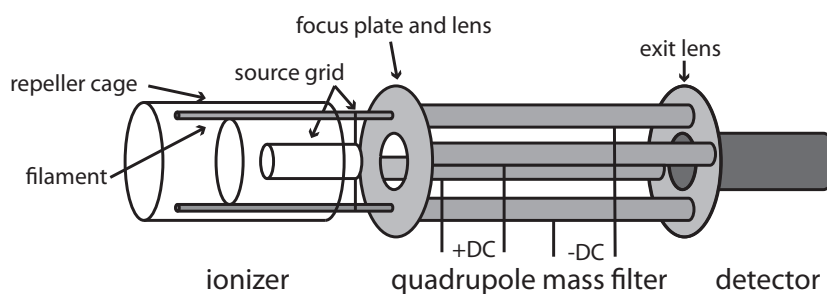

Fig. 3.13: Schematic image of a QMS.

4. Studies of the Pt(111) surface

The Pt(111) surface is a very well-studied surface. Here I will present som measurements which will serve as a background for the results presented in chapter 5. Furthermore, I will present *in situ* XPS data obtained on the CO oxidation over Pt(111). Simultaneously with the HPXPS measurements reactivity data were measured with the QMS.

4.1 The substrate

In surface science studies often single crystals are used. A crystal is a structure in which the atoms are arranged with a three dimensional periodicity, and in a single crystal structure all atoms follow the same crystal orientation. The bulk structure of Pt is the *face centred cubic* (fcc) crystal structure, which is one of the 14 *bravais* lattices. The surface under study will depend on how the crystal is cut, which is denoted using *miller* indices. The miller indices are (hkl), where h, k and l denotes the surface normal vector. In Figure 4.1(a) a fcc crystal is shown and the atoms are represented by the orange balls. In panel (b) the (111) plane is indicated by the greyed area. In panel (c) the fcc(111) surface is shown and the unit cell is indicated. The substrate used in my experiments is a Pt(111) crystal and is the surface represented in Figure 4.1(c).

4.2 Adsorption of CO and O on the Pt(111) surface

Saturation adsorption of CO on Pt(111) at room temperature results in a c(4x2) phase [34], as depicted in Figure 4.2(a) where the grey balls are Pt atoms which do not participate in the bonding. The unit cell contains two
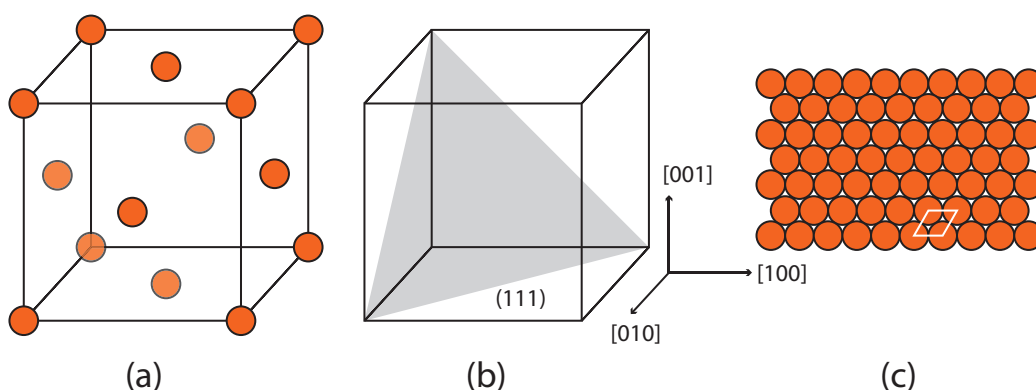
Fig. 4.1: The fcc(111) surface. (a) The fcc crystal. (b) The (111) plane. (c) The surface cut from the (111) plane, the unit cell is marked by the white romb.

molecules in on top and two in bridge sites, resulting in a coverage of 0.25 on top and 0.25 bridge sites compared to the Pt(111) support.

Adsorption of O_2 on Pt(111) at room temperature is followed by dissociation into atomic O. Electron energy loss spectroscopy (EELS) and LEED measurements perfomed by Steininger et al. [52] showed that the O atoms occupy threefold hollow sites in a p(2x2) phase. This symmetry has a saturation coverage of 0.25 monolayer (ML) and a ball model is shown in Figure 4.2(b) where the grey balls are Pt atoms which do not participate in the bonding. A monolayer is in this case defined as the ratio between O and Pt atoms when all available sites are occupied.

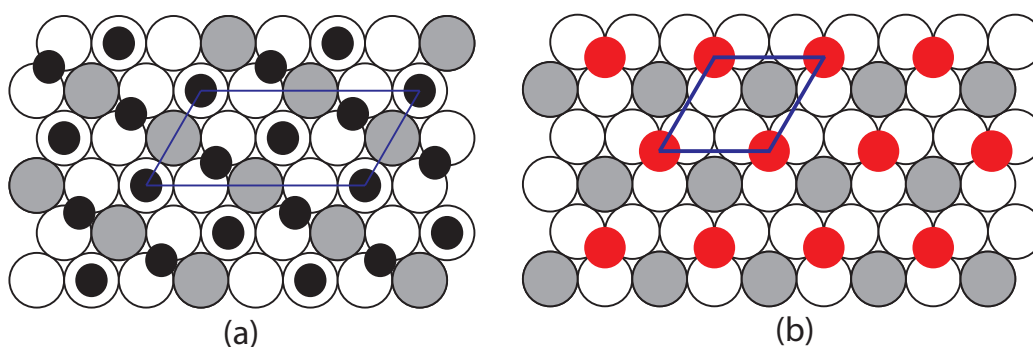**Fig. 4.2:** CO and O_2 adsorption on Pt(111). (a) CO on a Pt(111) surface. The black spots represent CO molecules and the circles represent the substrate atoms. The unit cell for the c(4x2) configuration of CO is marked. (b) A model of O adsorbed on Pt(111) is shown where the red balls represent O atoms. The p(2x2) unit cell is here marked by the blue romb. The grey balls represent Pt atoms which do not form bonds with the adsorbates.

4.3 XPS measurements on the adsorbate covered Pt(111) surface

XP spectra were acquired on the clean, CO-covered, and O-covered Pt(111) surfaces. The clean surface was obtained by cycles of Ar sputtering and O_2 treatments where the crystal was heated to 870 K in 10^{-7} mbar O_2 for 2 min followed by annealing at 1000 K for 5 min in UHV. CO and O_2 were subsequently dosed onto the clean Pt(111) surface. In Figure 4.3 the core levels for these preparations are shown. In panel (a) three Pt 4f spectra are shown corresponding to the clean, O-covered, and CO-covered Pt(111) surface. The bottom spectrum shows the Pt 4f spectrum for the clean Pt(111) crystal. Two peaks can be seen for each spin-orbit split level. The blue components at 74.3 eV and 71 eV are due to photoemission from bulk Pt, while the two other components at 73.7 eV and 70.4 eV are due to surface Pt. The
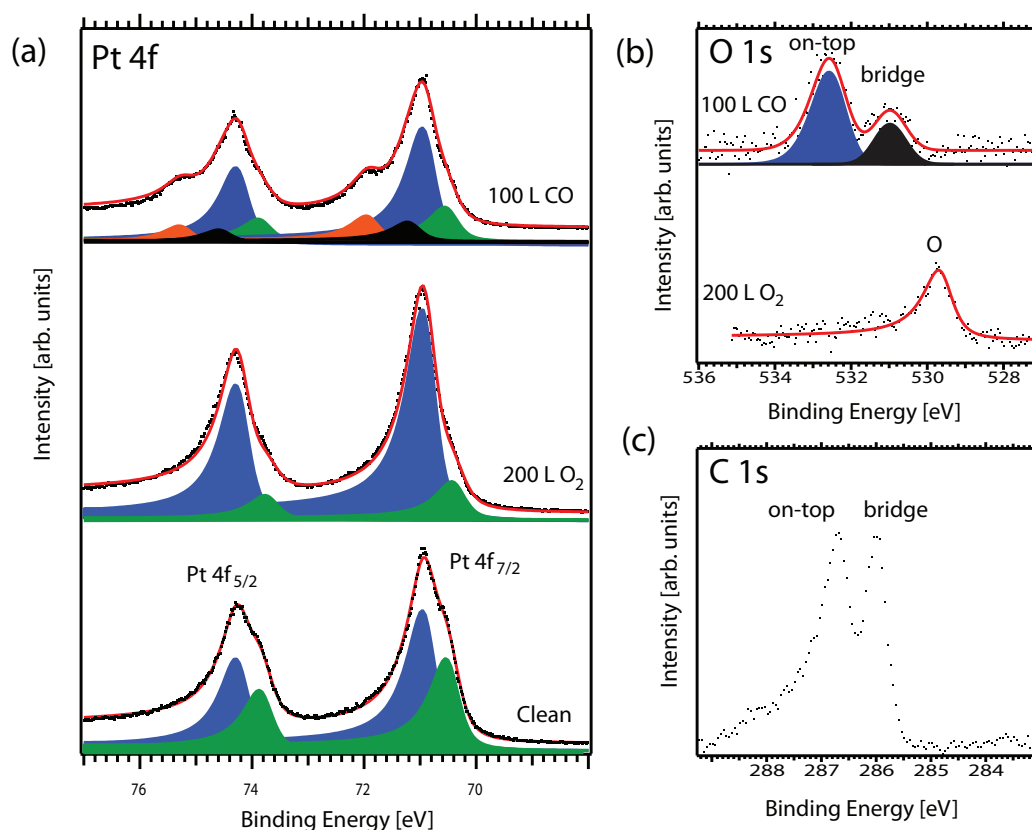

Fig. 4.3: Core level spectra acquired on the clean, O-covered and CO-covered Pt(111) surface. (a) Pt 4f core level. (b) O 1s level for 200 L O_2 and 100 L CO. (c) shows a C 1s spectrum for the CO/Pt(111) surface.

two different components are a consequence of the different coordination of surface and bulk Pt atoms. Each Pt bulk atom is coordinated to twelve other Pt atoms, while each Pt surface atom is coordinated to nine atoms, which is seen in the chemical shift. The middle spectrum was obtained on a Pt(111) surface exposed to 200 Langmuir (L)[1 L=10^{-6} Torr·s] O_2 at room temperature. The blue bulk components are not shifted. The green components have identical binding energies as the component assigned to Pt surface atoms on a clean Pt(111) surface. They are therefore assigned to surface Pt atoms which do not bind to O, cf. Figure 4.2(b). The Pt-O interface component is very close to the bulk Pt component and is not resolved in this spectrum. The topmost spectrum was acquired on the Pt surface exposed to 100 L CO at room temperature. Several peaks are observed. The bulk and surface components are still present and two additional components are observed in each spin-orbit split level. The components at 75.3 eV and 72.0 eV are assigned to the CO molecules in on top sites, while the components at 74.6 eV and 71.2 eV originate from the CO molecules in bridge sites. The spectrum was fitted using binding energies from Björneholm et al. [34].

In Figure 4.3(b) two O 1s spectra are shown, the upper for the Pt surface exposed to 100 L CO and the lower for the Pt surface exposed to 200 L O_2. For the upper spectrum, two peaks are observed at 532.6 eV and 531.0 eV originating from CO molecules in on top and bridge sites, respectively. In the lower spectrum, one peak is observed at 529.7 eV originating from the O atoms in the threefold hollow phase. Panel (c) shows a C 1s spectrum for 100 L CO/Pt(111), and two peaks at 286.7 eV and 286.0 eV are seen which correspond to adsorption in on top and bridge sites, respectively. The adsorption of CO and O nicely illustrates how XPS can be used to distinguish between different molecules as well as molecules in different adsorption sites.

4.4   Measurements of CO oxidation on Pt(111)

CO oxidation over Pt-based catalysts has been studied extensively since the work of Langmuir in 1922 [53]. He proposed that the oxidation mechanism was relatively simple: O_2 would hit the surface and dissociate, leading to atomic O bound to individual Pt atoms. When CO molecules from the gas phase hit the adsorbed O they would react, forming CO_2 according to the Eley-Rideal mechanism [cf. chapter 1 Figure 1.1(b)]. However, it is now well established that the oxidation instead goes through the Langmuir-Hinshelwood mechanism where a chemisorbed CO molecule reacts with dis-

sociatively adsorbed O on the surface and forms CO_2 [54] [cf. chapter 1 Figure 1.1(a)].

To investigate the reactivity of the Pt(111) surface, the crystal was cleaned as before and transferred into the HP cell. A gas mixture of O_2 and CO with an O_2:CO ratio of 9:1 was introduced at a total pressure of 0.25 mbar. The sample was heated while the gas composition was monitored by the QMS and XP spectra were recorded continuously.

In Figure 4.4, QMS and XPS data for the reaction are shown. The bottom graph shows the QMS data with the partial pressures for O_2, CO and CO_2. At 490 K a small increase of CO_2 partial pressure is seen; in the corresponding O 1s HPXPS spectrum the two peaks at 539.0 eV and 538.8 eV originate from gas phase O_2 [22] while the two peaks at 532.6 eV and 530.9 eV are assigned to CO molecules adsorbed in on top and bridge sites, respectively. The two O_2 peaks are due to *core polarisation*. In the ground state O_2 has valence spin S=1. After photoionisation the spin of the core hole couples to the valence
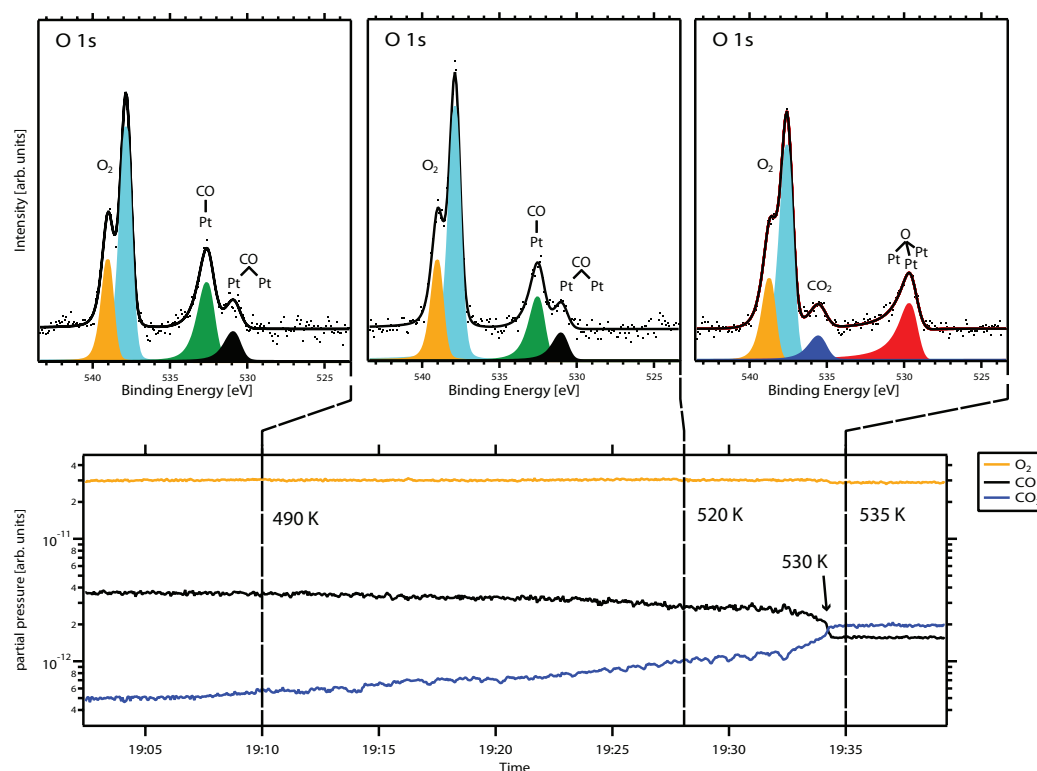

Fig. 4.4: Spectra showing QMS and XPS data. The bottom graph shows QMS data acquired while heating the sample in a total pressure of 0.25 mbar. The three top spectra are acquired *in situ* at the points marked in the QMS graph.

spin creating two final states with J=1/2 and J=3/2, respectively [22]. This is a nice illustration of the fact that in XP spectra the final state is seen, not the initial state.

When the temperature is increased, the QMS data show an increase in CO_2 partial pressure while the CO partial pressure drops. In the XP spectra acquired at 520 K the CO/Pt peaks at 532.6 eV and 530.9 eV are still visible. The $CO:O_2$ signal ratio is decreased by 29% compared to the 490 K spectrum, which is attributed to desorption of CO due to the increased temperature. At 530 K the partial pressures of CO and CO_2 change quickly and become inverted relative to each other; a small decrease in O_2 partial pressure is also observed. At this point, the active CO oxidation starts and the XP spectrum recorded at 535 K shows that the O_2 gas phase peak is still present, but the peaks assigned to adsorbed CO have vanished. Instead a peak is observed at 535.6 eV. Comparing with the O 1s spectrum of oxygen covered Pt(111) I assign this new peak to O atoms bound in threefold hollow sites at the Pt surface as discussed earlier.

In summary, my experiments of CO oxidation in a 1:9 $CO:O_2$ gas mixture at a total pressure of 0.25 mbar shows the following:

- Below 535 K the Pt(111) is poisoned by CO which is adsorbed in the c(4x2) structure; the reactivity of the surface is low.

- Above 535 K the Pt(111) surface suddenly shifts to an oxygen covered phase, with atomic oxygen adsorbed in a p(2x2) structure. This phase has a much higher reactivity as compared to that of the c(4x2)-CO/Pt phase, and active CO oxidation is observed.

These results are consistent with literature [54, 55].

The HPXP spectra shown in Figure 4.4 show gas phase molecules as well as adsorbed species. This shows that the use of HPXPS in combination with mass spectrometry is an extremely powerful tool to study catalytic reactions at operation conditions. If larger molecules are used, such as styrene, it should be possible to evaluate the reaction steps from the chemical shifts in the XPS data. The reaction measurements performed here confirm the well-established model for CO oxidation on Pt(111). As mentioned before, CO oxidation has been studied extensively in numerous experiments. Nevertheless, the present experiment demonstrates the possibility of performing reaction measurements for catalysis studies using the HPXPS instrument at beamline I511.

5. The FeO(111) bilayer grown on Pt(111)

Vurens et al. were the first to grow a thin iron oxide film on the Pt(111) surface in 1988 [56]. The experiment demonstrated the concept of creating oxide films on nobel metals to allow for oxide surfaces studies. The motivation for growing thin oxide films is that metal oxides surfaces are more difficult to study compared to metal surfaces due to problems with preparation, cleaning, and the difficulty in using electron spectroscopy on the often insulating surfaces. Further, thin oxide films have received much attention as they exhibit properties different from those of their bulk counterparts [57] with possibilities for creating novel materials.

FeO has been studied extensively along with other metal oxides. In 1993, Galloway et al. [58] showed by STM that a monolayer FeO film exhibits a bilayer structure. This bilayer FeO has then been subject of numerous studies, which include the reduction by atomic hydrogen [57], CO oxidation [59] and styrene synthesis [60]. In this chapter, the previously known structure of the bilayer FeO film will be presented. I will present LEED and XPS data acquired during the experiments.

5.1 Structure of the FeO(111) bilayer on Pt(111)

FeO grown on Pt(111) has a lattice constant of 3.1 Å [61], which is 12% larger than that of the Pt(111) support (2.78 Å). Also, the FeO lattice is slightly rotated, 0.6° [57], with respect to the Pt(111) surface. This mismatch gives rise to a moiré superlattice with a $(\sqrt{91}\mathrm{x}\sqrt{91})\mathrm{R}5.2°$ unit cell [57]. Figure 5.1 shows a ball model of the FeO(111) structure suported by Pt(111). In panel (a) a side view of the structure is shown and the bilayer structure is clearly seen as Fe and O atoms form separated layers. A top view is shown in panel
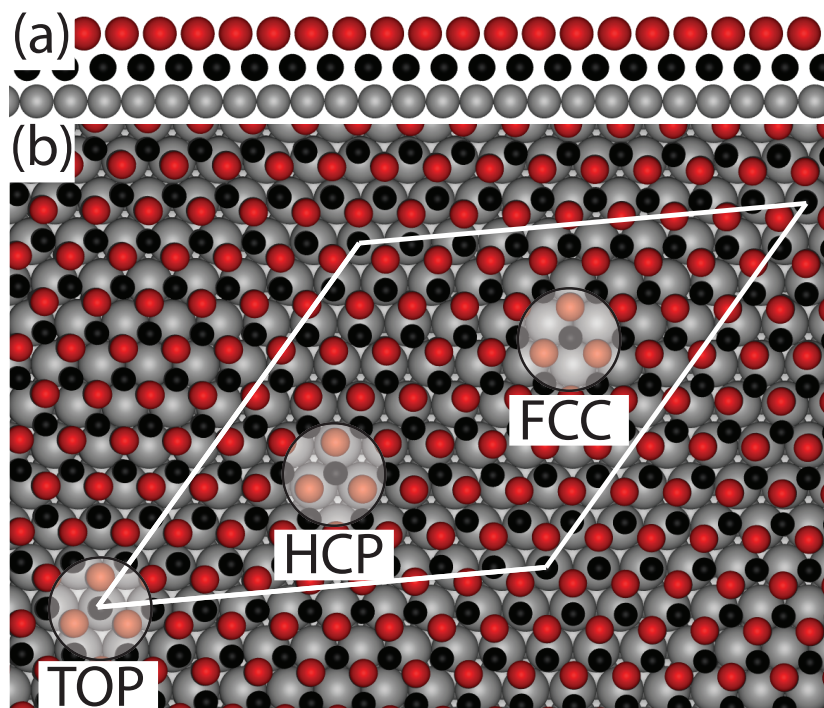
Fig. 5.1: Ball model of the Pt(111) surface covered by a bilayer FeO film. The grey balls represent the Pt(111) substrate, the black balls are Fe atoms and the red balls are O atoms. In (a) a side view of the system is shown and in (b) a top view is shown. In (b), the $(\sqrt{91}\text{x}\sqrt{91})\text{R}5.2^o$ unit cell is marked as the white romb and the effects of the missmatch, the moiré superlattice, is clearly visible as the brighter spots. Three high symmetry domains are also marked.

(b) where the moiré unit cell is indicated by the white romb. Also marked in panel (b) are three different high symmetry regions which arise from the stacking of the bilayer with respect to the substrate.

An FeO(111) film that covers the entire Pt(111) surface will have a Fe and O atom density of 0.8 compared to the Pt surface [cf. Figure 5.1(b)]. A monolayer may then be defined in different ways, e.g. by atom density. However, in this report, a 1 ML FeO(111) film is defined as when a perfect bilayer covers the entire Pt(111) substrate.

Growth of FeO and Fe on Pt(111)

For this study, coverage control of the FeO(111) film was important and some time was used to calibrate the coverage in the XPS setup. Metallic iron has a 3D dendritic growth mode on Pt(111) and it is thus difficult to control the Fe coverage directly by following the reduction of the Pt(111) surface

component with XPS. In contrast, FeO grows layer-by-layer up to a coverage of at least 2.1 ML [62]. It is easy to find the coverage of an FeO(111) film that partly covers the Pt(111) substrate if CO adsorption is used as a probe. CO does not adsorb on FeO(111) at room temperature, but forms a c(4x2) structure on the uncovered Pt(111). This makes CO an excellent probe for coverage calibration up to 1 ML. Beyond the first monolayer it is harder to calibrate the FeO coverage since CO does not adsorb anymore, and other methods are required.

In my experiments, the film was grown by first sublimating metallic Fe onto the sample at room temperature for 5 minutes inside the UHV chamber. The deposited metallic Fe was then oxidised by heating the sample to 870 K in $1 \cdot 10^{-6}$ mbar O_2. Oxygen dosing was started when the sample temperature reached 650 K. After oxidation at 870 K for 2 min, the sample was cooled down to 650 K in oxygen before it was pumped down to UHV again. CO was dosed at room temperature to calibrate the coverage. For 1 ML, additional Fe was evaporated for 3 minutes followed by an identical oxidation cycle.

Coverage calibration using the C 1s line

The FeO(111) coverage of sub-monolayer films can be extracted by comparing the C 1s signal from a CO saturated clean Pt(111) surface with a corresponding signal from a CO saturated Pt(111) surface partly covered by FeO(111). The ratio between these two signals corresponds to the uncovered Pt(111) surface and the FeO coverage can therefore be calculated as

$$\theta_{FeO} = 1 - \frac{I_{\text{C 1s, FeO}}}{I_{\text{C 1s, Pt(111)}}}, \tag{5.1}$$

where θ_{FeO} is the coverage of FeO. $I_{\text{C 1s, FeO}}$ and $I_{\text{C 1s, Pt(111)}}$ are the integrated C 1s signals of a CO-saturated clean and partly FeO-covered Pt(111) surface, respectively. Figure 5.2(a) shows the C 1s spectra from CO-saturated Pt(111) surface, uncovered (lower) and partly covered (upper) by FeO. Two distinct peaks are observed in each spectrum and they are assigned to the CO adsorbed in bridge and on top sites [cf. Figure 4.3(c)]. A polynomial background was removed before normalisation to beam current and dwell time. The integrated C 1s signal of the partly FeO-covered surface corresponds to 30% of the C 1s signal of a CO saturated Pt(111) surface. Using formula (5.1) it is found that the FeO coverage is 0.7 ML.

The strength of this method is that it is easy to handle and thus works well as a first approximation during the experiments. On the other hand, the
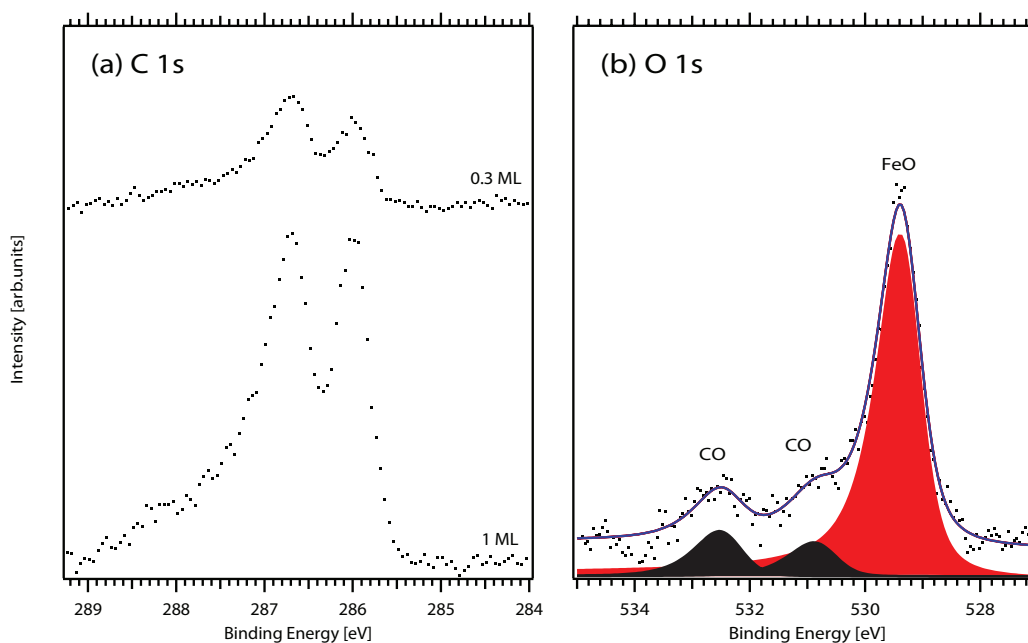
Fig. 5.2: Spectra used for calibration of FeO coverage. (a) shows C 1s spectra for two different CO satu-
rated surfaces, a clean Pt(111) and a FeO(111)/Pt(111) surface. (b) shows the O 1s spectrum
of the same FeO(111)/Pt(111) surface as seen in (a).

normalisation of XPS data might introduce systematic errors. The intensity
of the light is linearly proportional to the beam current, although experiments
have shown that this is not always true. The reason for this is unknown,
but it might be due different beam positions for different beam currents.
This uncertainty in intensity makes it hard to quantitatively compare spectra
acquired at different beam currents.

Coverage calibration using the O 1s line

The FeO coverage can also be found using the O 1s XP spectrum. The main
advantage with this method is that the FeO coverage can be determined using
one spectrum only. Normalisation that might introduce systematic errors is
not necessary. Figure 5.2(b) shows an O 1s spectrum of a Pt(111) surface
partly covered with FeO(111) after CO exposure at room temperature. The
peaks marked CO with binding energies 532.5 eV and 530.9 eV originate from
CO molecules in on top and bridge sites, respectively [cf. Figure 4.3(b)] [34].
The third peak at 529.3 eV I assign to photoemission from the O atoms
in FeO [57]. There is quite a large intensity difference, and the FeO peak
holds 86% of the signal. This is partly due to different amounts of O in the

respective unit cells. As discussed earlier the number O for FeO is 0.8 O atoms per Pt atom, while it is 0.5 O atoms per Pt atom for CO adsorbed on Pt(111), 0.25 for on top and 0.25 for bridge sites, respectively. The approach used here is to normalise the spectral intensity to the number of O atoms per Pt atom for the different structures. The normalisation constants are found from the inverse Pt to O ratio. Thus 1/0.8=1.2 is the normalisation constant for FeO and 4 for CO in both on top and bridge sites. The coverage can then be calculated as

$$\theta_{FeO} = \frac{1.2 I_{FeO}}{1.2 I_{FeO} + 4 I_{CO_{on-top}} + 4 I_{CO_{bridge}}}, \tag{5.2}$$

where θ_{FeO} is the sub ML coverage of FeO and the I's are the integrated signals from the respective peaks. By inserting the integrated signals from the components in Figure 5.2(b) into Eq. 5.2 it is found that the FeO coverage is 0.61 ML.

Comparison of the calibration methods

Obviously, the different methods gave different coverages, 0.7 ML usint the C 1s line and 0.61 ML using the 0 1s line yielding a mean coverage of 0.66 ± 0.064 ML. The method using C 1s intensities gave a FeO coverage of 0.7 ML and the method using O 1s gave 0.61 ML. The C 1s method is indirect and involves normalisation of XPS data, which can be difficult. However, the O 1s method is direct and normalisation is not an issue. As a result, the coverage to be used is that from the O 1s method.

The coverage calibration for 1 ML FeO films is easier. By evaporating Fe and oxidizing it in cycles with CO dosing in between cycles, a coverage of 1 ML is achieved when the C 1s signal has vanished completely.

5.2 Characterisation of the FeO(111) bilayer

Long-range order investigation with LEED

As described earlier LEED is a good technique for determining surface symmetries. It is an important complement to XPS from which it is difficult to extract direct structural information and long-range order is lacking. Figure 5.3(a) shows a LEED image of the 1 ML FeO film where the main diffraction spots of Pt and FeO are observed. Around the FeO diffraction spots

a number of satellites are observed as a result of the moiré superstructure. The appearance is explained by double diffraction between the support and overlayer [60] with the relation between the lattices given by $\vec{q}_M = \vec{q}_O - \vec{q}_S$, where $\vec{q}_M$, $\vec{q}_O$ and $\vec{q}_S$ are reciprocal space vectors for the moiré pattern, overlayer and substrate, respectively [63]. In panel (b) a cross section of the LEED image is shown, represented by the white line in panel (a). By fitting Gaußian functions to the peaks, the relative distance between them and thus the magnitude of reciprocal lattice vectors can be found. From Figure 5.3(b) it is found that the lattice constant of FeO is 1.10 ± 0.034 times larger than that of Pt, in agreement with the literature value (1.12).
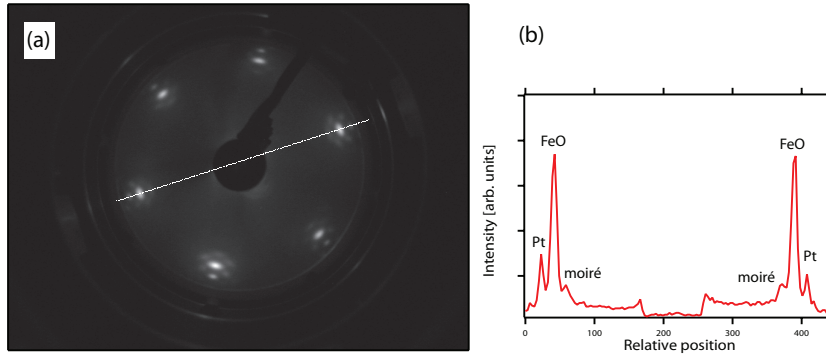
Fig. 5.3: LEED on the 1 ML FeO film. (a) LEED image of a Pt(111) surface covered by FeO(111). The rosette pattern given rise to by the moiré structure is clearly seen. (b) a cross section of the LEED is shown as marked by the white line in (a).

Core level XP spectra of FeO(111)

In Figure 5.4 core level spectra are shown for the two films the growth of which was already discussed in section 5.1. The two upper spectra in panels (a) and (b) are from the 0.61 ML film while the three lower are from the 1 ML film. In panel (a) the O 1s spectrum of the 0.61 ML preparation is shown. A peak is seen at 529.5 eV. In panel (b) a Pt 4f spectrum is shown with four visible peaks. The peaks denoted A and B correspond to the spin-orbit split 5/2 and 7/2 bulk components at binding energies 74.3 eV and 71 eV, respectively. The components denoted C and D are the surface components, which are shifted 0.57 eV towards lower binding energy compared to their respective bulk peak. The energies of the bulk peaks are the same as already reported for the clean Pt(111) surface. Here the surface is partly covered by FeO. This leads to fewer Pt surface atoms resulting in the observed lowered intensity for the surface Pt peaks. The Fe-Pt interface peaks are not seen as they coincide with the bulk peaks.

In Figure 5.4(c) the O 1s peak for 1 ML is seen at 529.4 eV, and in panel (d) the bulk peaks are seen at the same positions as for 0.61 ML, 74.3 eV and 71 eV for A and B, respectively. The surface peaks C and D are shifted 0.63 eV towards higher binding energy. As the surface is covered completely, the surface Pt peaks have vanished and additional peaks are seen instead. The Fe 3p spectrum of 1 ML FeO is presented in panel (e) where a clear Fe 3p peak is seen to the left of the Pt 5p peak. Unfortunately, no Fe 3p spectrum was recorded of the 0.61 ML FeO film.
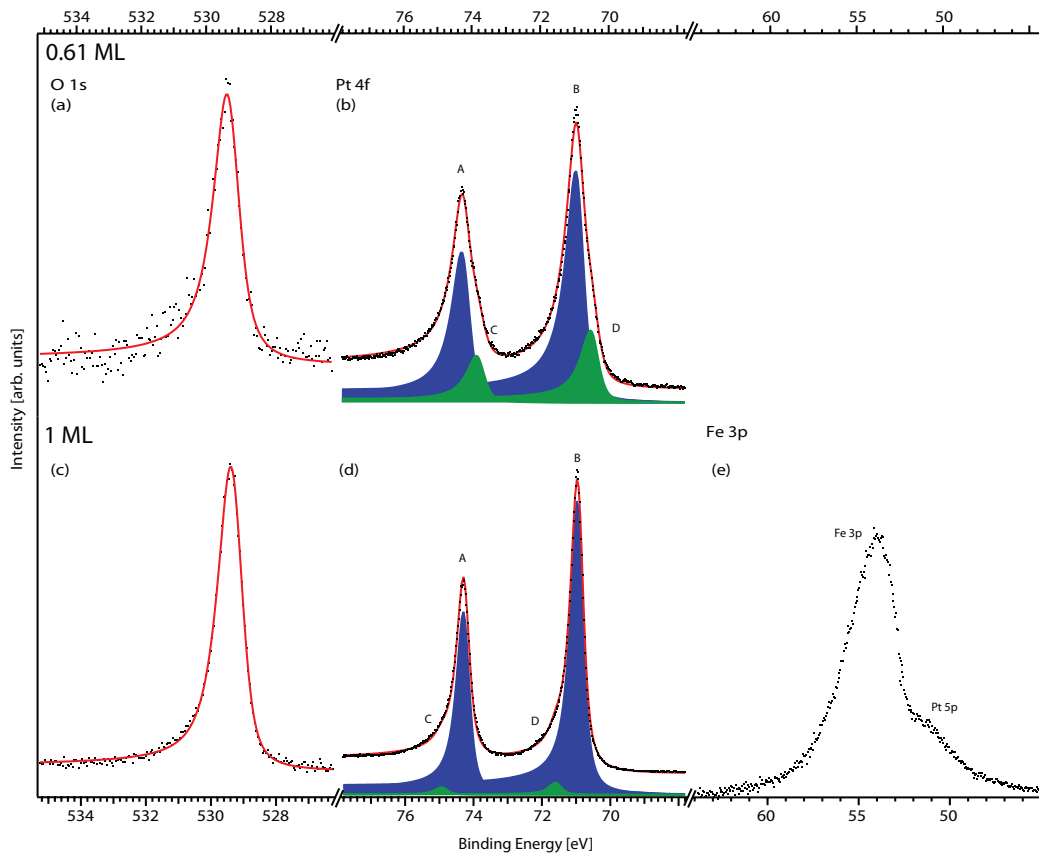

Fig. 5.4: Core level spectra for the two different coverages of bilayer FeO. The two upper spectra are acquired from the 0.61 ML FeO film while the three lower are from the 1 ML FeO film.

Comparing the spectra for the 0.61 ML film and the 1 ML film the major difference is observed in the Pt 4f spectra. In Figure 5.4(b) the Pt surface peak of the uncovered Pt is clearly visible. In Figure 5.4(d) the original surface peaks have vanished as the Pt substrate is completely covered by FeO. A Pt $4f_{7/2}$ peak at a similar binding energy was previously seen by Miller et al. when studying O adsorption on Pt(111) in near ambient pressures and elevated temperatures [64]. The peak was attributed to a surface oxide

composed of PtO_4. It is unlikely that this is the case for my experiments as pressures of a few mbar was required for achieving the higher degree of oxidation. However, the observation of a corresponding peak here points towards defects in the bilayer film.

6. The FeO$_2$(111) Trilayer Structure

The trilayer FeO$_2$ film was first observed by Sun et al. in a reactivity study in 2009 [59] in which they studied the increased CO oxidation rate over a FeO film in high CO and O$_2$ partial pressures. The original FeO film reconstructed into a film with a Fe:O ratio close to two. LEED showed that the long-range order of the O enriched film was close to that of pristine FeO(111)/Pt(111). It was believed that this new structure was the active oxidant, and in view of the immense importance of the CO oxidation reaction this film became the subject of STM and *density functional theory* (DFT) studies in which the growth and reactivity of the film was studied *ex situ*. Although studied by STM and DFT, no extensive XPS studies have been performed of the trilayer. In the following I first present the structural and reactivity aspects of the previous STM and DFT studies [65–68], and thereafter I will present my own LEED and XPS results.

6.1 Literature survey: Results from previous investigations

Oxidation of the FeO(111) bilayer film

The transformation of the iron oxide film from a bilayer into a trilayer structure was investigated by Sun et al. [68]. DFT calculations were performed for the on top symmetry region of the FeO$_2$ unit cell, and a reaction path was suggested which is shown in Figure 6.1. In panel (a) the bilayer FeO surface is exposed to a 20 mbar pressure of O$_2$ which chemisorbs on an Fe atom, slightly pulling it out from the surface [panel (b)]. Electrons are then transferred from the oxide to the chemisorbed oxygen and O$_2^{2-}$ is formed [panel (c)]. This peroxide anion binds to a neighbouring Fe atom [panel (d)] and pulls it up. This inverts the film and a trilayer is formed [panel (e)].
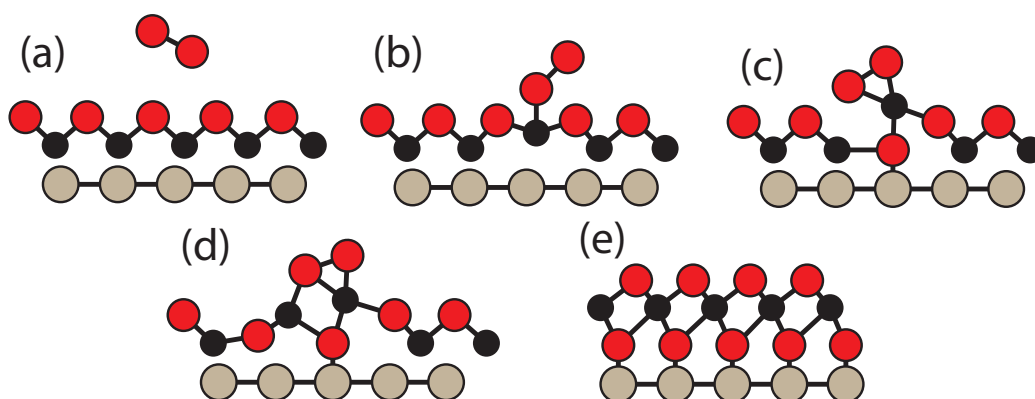
Fig. 6.1: The trilayer oxidation as suggested in [68]. The grey balls represent Pt atoms, the black- and red balls represent Fe and O atoms, respectively.

Structure of the trilayer FeO$_2$(111) film

In the literature it is suggested that the structure of the trilayer film is very similar to that of the bilayer. The arrangement of the O atoms beneath the Fe layer should follow that of the Fe lattice, as O binds stronger to Fe than to Pt. Figure 6.2 shows a ball model of the trilayer film. In panel (a) a side view is shown, where the trilayer structure is clearly visible. In panel (b) a top view of the surface is shown. Three high symmetry regions are observed. The white romb in the figure shows the $(\sqrt{91}\mathrm{x}\sqrt{91})\mathrm{R}5.2°$ moiré unit cell. Giordano et al. [65] found an increase in the size of moiré supercell, which points towards a decrease in lattice constant. Indeed, it was found that the trilayer lattice constant should be 3.05 Å compared to 3.1 Å as for FeO. In order to keep the moiré structure, the contraction must be accompanied by a rotation which is unknown. Due to this, the FeO lattice was used as model structure for the trilayer. However, this ball model does not represent the real film as it has been shown that the film consists of oxygen rich trilayer islands with a $(\sqrt{3}\mathrm{x}\sqrt{3})\mathrm{R}30°$ structure rather than a continuous film [65]. Calculations in [66] showed that the trilayer oxidation is domain specific. The oxidation of the bilayer occurs in the on top symmetry regions for O on Pt, which would account for the O rich islands.

CO Oxidation by the trilayer FeO$_2$ film

The oxidation of CO over FeO$_2$ was studied by STM by Lewandowski et al. [66] who exposed the trilayer film to CO and characterised it in UHV. It was found that the film indeed had been reduced. It was concluded that
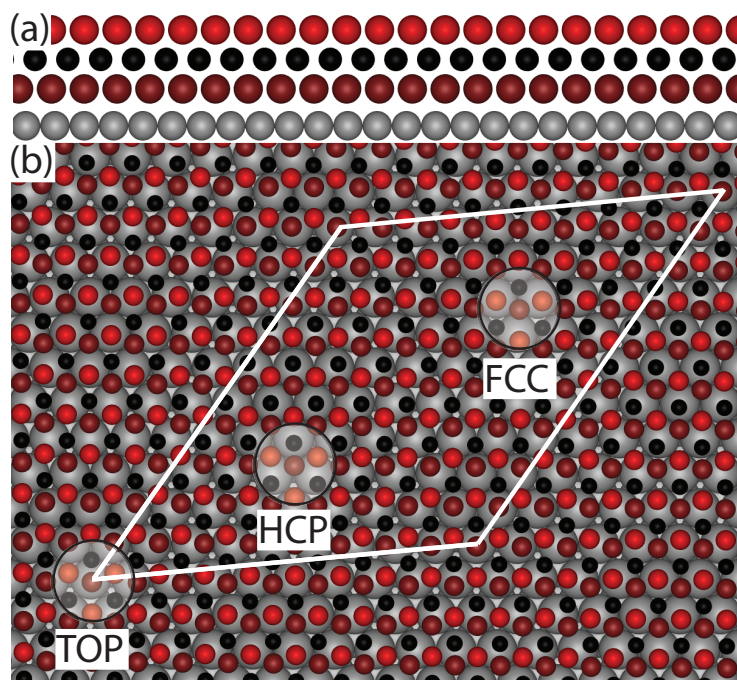
Fig. 6.2: A ball model of the suggested trilayer FeO$_2$ structure. (a) The trilayer shown from the side. (b) a top view of the FeO$_2$ film. The three different high-symmetry domains are still present and marked in the figure. The grey- and black balls represent Pt and Fe respectively. The dark red balls represent the interface O and the red balls represent the surface O.

the CO oxidation over FeO$_2$ would follow the Mars-van Krevelen mechanism [cf. chapter 1 Figure 1.1(c)]. Additionally, it was found that it was possible to re-oxidise the reduced film into a trilayer. If this is the case, it should be possible to obtain a catalytic reaction using a CO and O$_2$ gas mixture as proposed in Figure 6.3. The CO molecules are oxidised into CO$_2$ via the Mars-van Krevelen mechanism, thus reducing the trilayer. The O$_2$ molecules then react with the reduced part of the film and oxidise it back into a trilayer.
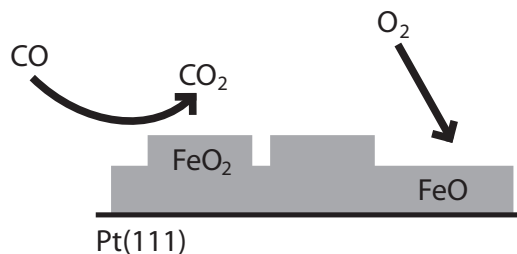

Fig. 6.3: The proposed reaction mechanism. CO will reduce the trilayer film, which the O$_2$ molecules will oxidise into a trilayer again.

The reaction is proposed to start at lower temperatures than over Pt, $\sim$450 K instead of $\sim$530 K, which opens up for the use of trilayer oxides to promote low temperature oxidation reactions over noble metals.

6.2 Creating the Trilayer

In Figure 6.4 three graphs are shown which contain the *in situ* data for the oxidation of the 0.61 ML bilayer FeO(111) film. The film was oxidised by dosing O$_2$ at a flow of 2 cm^3/min and a pressure of 0.6 mbar in the HP cell. While the sample was heated up to 500 K, and XP spectra were recorded continuously during the oxidation process. In panel (a) four O 1s spectra acquired at different temperatures are seen. In the bottom spectrum an O 1s peak is observed at 529.7 eV with a shoulder towards higher binding energy. As the main peak at 529.7 eV is close to the position of the O 1s bilayer FeO(111) peak at 529.5 eV [cf. Figure 5.4(a) and (c)] I assign the 529.7 eV peak to FeO similar to the bilayer. As the temperature is increased, the shoulder at the high energy side grows and another peak appears. Addition-

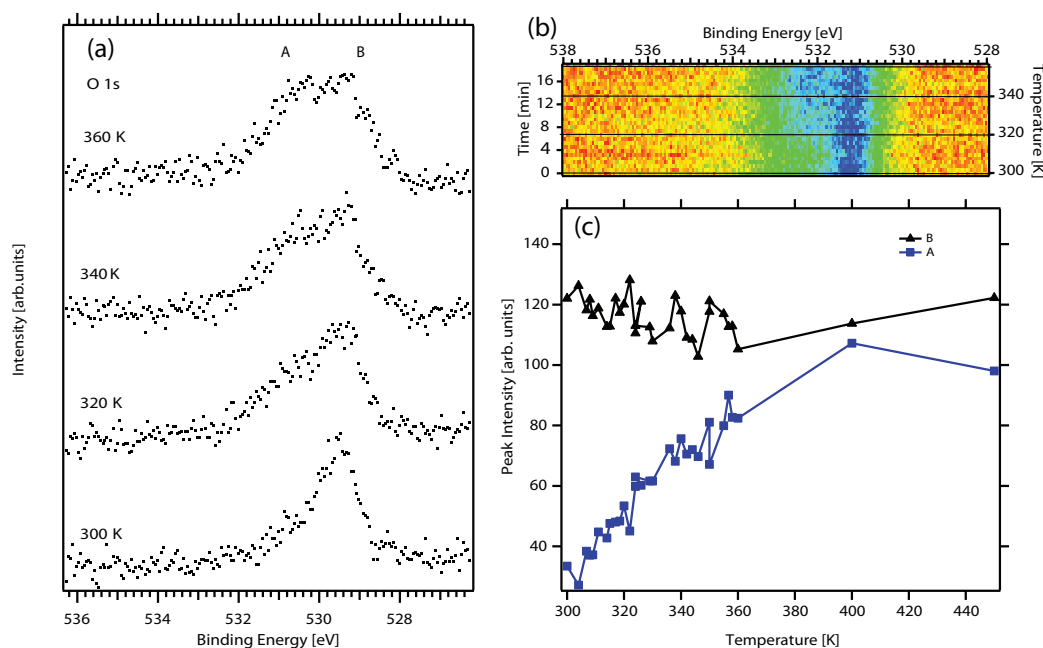**Fig. 6.4:** Trilayer oxidation of the 0.61 ML FeO film. (a) Selected O 1s spectra acquired at high pressure at different temperatures. (b) Surface plot of all O 1s spectra acquired during oxidation. The black lines are the spectra seen in (a). (c) The integrated intensities for the two components are shown as a function of temperature. A and B refer to the high and low energy peaks, respectively.

ally, the original peak at 529.7 eV shifts towards lower binding energy, while the new peak shifts towards higher binding energy as it grows. The high and low energy peaks are denoted A and B, respectively. Panel (b) shows a surface plot created from all O 1s spectra acquired during oxidation. In panel (c) the integrated peak intensities are plotted as a function of the sample temperature. The intensity of peak A increases continuously while the intensity of B drops slightly. For the fully oxidised film, the intensity of the A and B components are nearly identical. This suggests that the amount of O on the surface is doubled, as compared to the initial FeO coverage, and an FeO$_2$ film is obtained. The 1 ML FeO(111) bilayer film was oxidised in a similar manner.

6.3 Peak assignment

To assign the A and B components discussed above, angle resolved XPS was used. The FeO$_2$ film is stable in UHV and therefore it could be transferred to the UHV manipulator after pumping down the HP cell. The sample was rotated and electrons were collected at different emission angles. The surface sensitivity is enhanced at high emission angles with respect to the surface normal, and the origin of the peaks can be determined. The O 1s spectra for different emission angles are shown in Figure 6.5(a). In panel (b) the ratios between the integrated peaks are presented and plotted as a function of the emission angle. It is seen that the ratio decreases with emission angle. The decreased ratio B/A indicates that peak A is due to photoemission from the surface species. In contrast, species B is closer to the bulk [cf. Figure 6.5(c)]. It should be noted that the O 1s interface component is observed at 1.1 eV higher binding energy as compared to the surface O 1s peak on trilayers formed on Rh(100) [69], which is in disagreement with my results.

6.4 Symmetry analysis of the trilayer by LEED

In Figure 6.6 two LEED images are shown. In panel (a) the LEED image of the 0.61 ML FeO$_2$ film is shown and two structures are indicated. The vectors marked $\mathbf{a}_1^*$ and $\mathbf{a}_2^*$ are the reciprocal lattice vectors of the Pt surface. Two other vectors $\mathbf{b}_1^*$ and $\mathbf{b}_2^*$ are half the length of that of the Pt vectors. These vectors indicates that the overlayer real space unit cell has a (2x2)
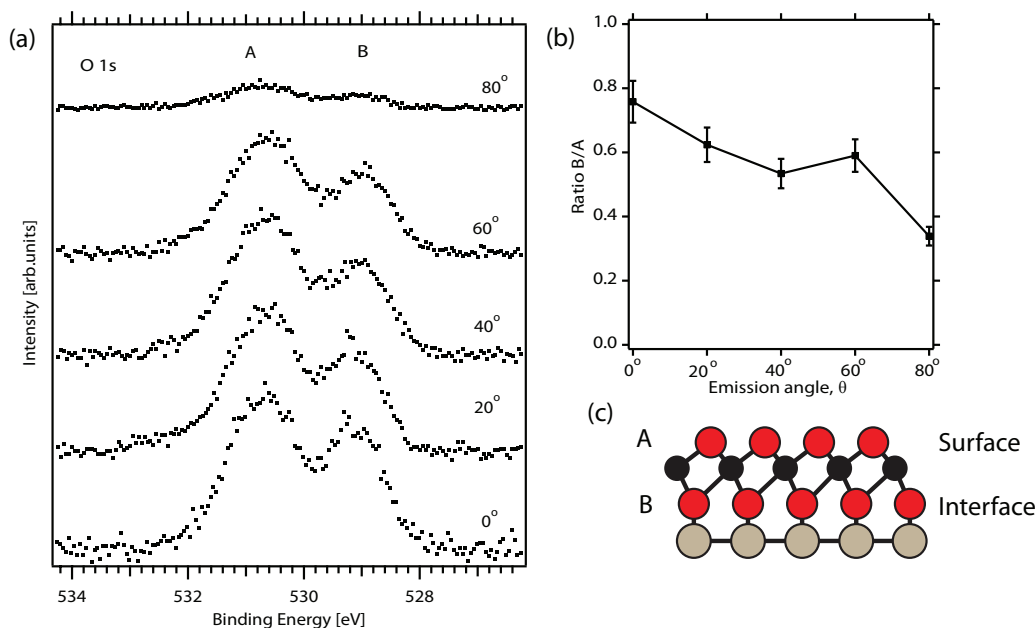
Fig. 6.5: Spectra for peak assignment. (a) different O 1s spectra acquired at different emission angles. (b) the ratio between the integrated intensities and in (c) the origin of Peak A and B is shown.

symmetry. Therefore, the (2x2) structure is assigned to O adsorbed on the FeO$_2$ uncovered Pt similar to O adsorption on clean Pt(111) as discussed above [cf. Figure 4.2(b)]. Indeed, adsorption of oxygen on the surface is expected since the sample has been exposed to large amounts of oxygen and it is not entirely covered by FeO$_2$.
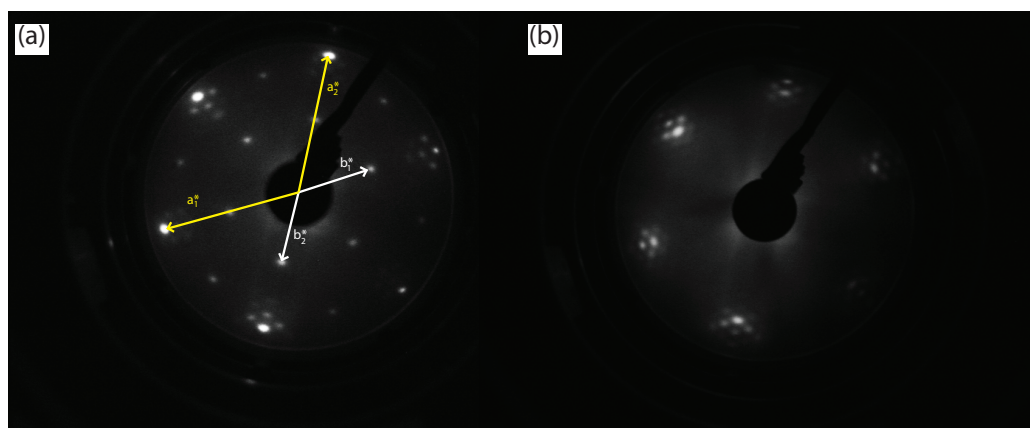

Fig. 6.6: LEED images of the two surfaces. In (a) LEED pattern for a 0.61 ML film is shown while in (b) the LEED pattern for the 1 ML film is shown. In (a) the reciprocal lattice vetors for the substrate and an overlayer is marked.

Diffraction from the FeO$_2$ film is observed as the rosette patterns surrounding the Pt diffraction spots, cf. Figure 6.6(a). The similarity to the LEED pattern of FeO [cf. Figure 5.3(a)] suggests that the bilayer and trilayer iron oxide have very similar in-plane structure.

The LEED pattern shown in Figure 6.6(b) was obtained on the 1 ML FeO$_2$ film. The p(2x2)-O pattern seen in panel (a) is not present in panel (b) as the entire surface is covered by FeO$_2$ so that no O can adsorb. Similar to panel (a), the rosette structure assigned to FeO$_2$ is observed. In both cases, analysis of the reciprocal lattice vectors shows that the FeO$_2$ film is expanded by 10% compared to the Pt surface. This is in disagreement with literature were a contraction of the lattice constant was observed [65].

6.5   Core level characterisation of the trilayer

As the trilayer film is stable under UHV conditions it is possible to obtain high resolution XP spectra on the FeO$_2$ trilayer films in UHV after the high pressure treatment. Figure 6.7 compares core level spectra for the 1 ML bilayer FeO and 1 ML trilayer FeO$_2$ films. The upper part of the figure shows the bilayer spectra and the lower part shows the spectra obtained on the trilayer.

Starting with the O 1s spectrum of the FeO$_2$ film in panel (d) I observe three different components at 530.9 eV (grey), 529.4 eV (black), and 528.9 eV (orange). As discussed when analysing the growth of the FeO$_2$ film, the grey and orange components are assigned to O atoms in the FeO$_2$ surface and interface layer, respectively. The black component has a binding energy of 529.4 eV, which is similar to that of O 1s in FeO [panel (a)], and it is therefore assigned to unoxidised patches of FeO.

Moving on to the Pt 4f spectra in panel (e), three components for each spin-orbit split level are observed. The components (blue) at 74.3 eV and 71.0 eV are assigned to bulk Pt as they have the same binding energy as the components assigned to bulk Pt for the bilayer [cf. panel (b)]. The values also compare favourbly with those found for the bulk Pt components of clean Pt(111) [cf. Figure 4.3(a)]. Further, the components (green) at 74.9 eV and 71.6 eV are assigned to photoemission of the defects observed for the bilayer film [panel (b)] as they have similar binding energies. The last component pair (orange) at 74.5 eV and 71.2 eV are not observed for the bilayer. Therefore, the orange components are assigned to photoemission

from the Pt-FeO$_2$ interface Pt atoms.

Comparing the Fe 3p spectra for the bilayer and trilayer, panels (c) and (f), reveals a shift in the binding energy from 54.8 eV (bilayer) to 55.2 eV (trilayer). This is consistent with oxidation of Fe and suggests that the Fe in FeO$_2$ is more oxidised as compared to FeO.

In conclusion, the XPS signature of the trilayer FeO$_2$ film has been identified as: (i) the appearance of an additional peak in the O 1s spectrum at 530.9 eV, (ii) a Pt-FeO$_2$ component in the Pt 4f$_{7/2}$ spectrum at 71.2 eV, and (iii) a positive shift of 0.3 eV in the Fe 3p line.
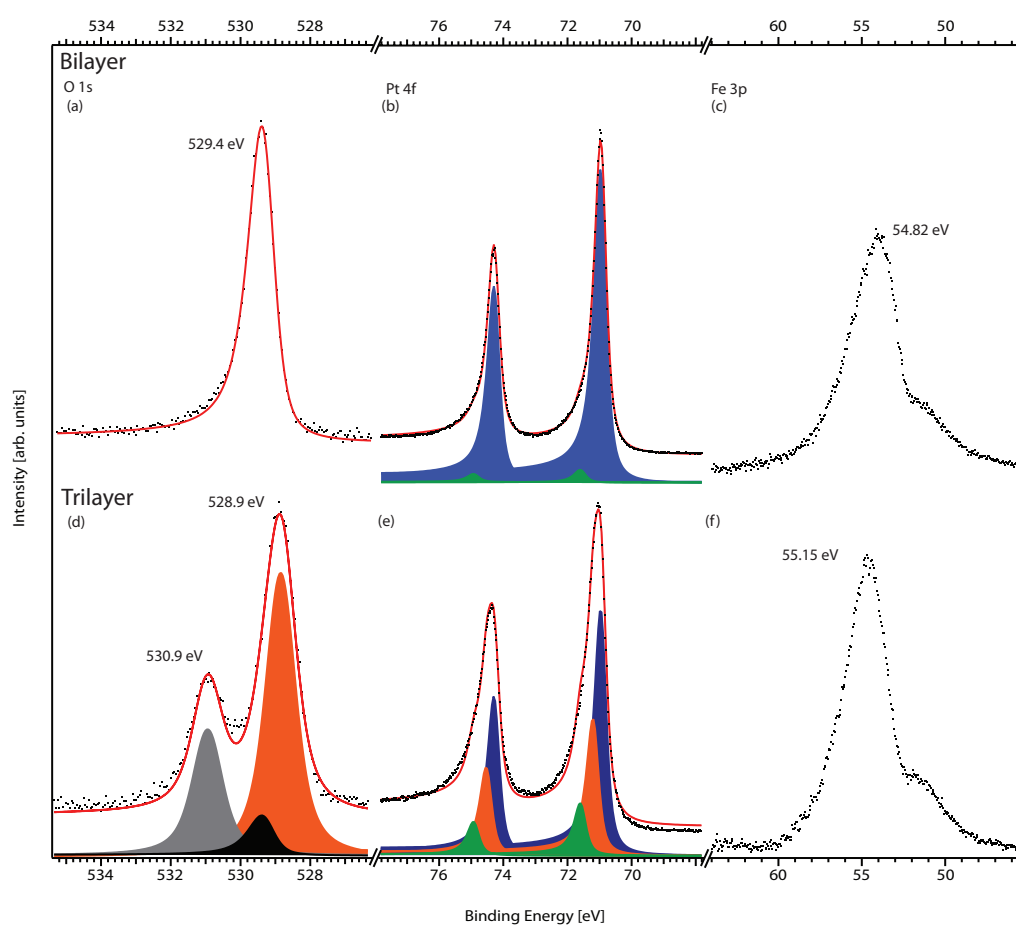

Fig. 6.7: Core level spectra for bilayer and trilayer. The spectra are shown for bilayer and trilayer in the upper and lower part of the figure, respectively.

Comparison between a 0.61 ML and a 1 ML FeO$_2$ film

Figure 6.8 shows core level spectra for the 0.61 ML and 1 ML trilayer preparations. The upper spectra show the core level spectra for the 0.61 ML preparation, while the lower spectra are for the 1 ML preparation. The binding energies of selected components are listed in Table 6.1.

For the 0.61 ML preparation it is clear that parts of the Pt(111) surface are not covered by iron oxide. Since the surface was exposed to O$_2$ at high pressure, a p(2x2)-O structure is expected to cover the uncovered Pt(111) patches. As discussed above this p(2x2)-O structure should have a surface Pt component at 70.4 eV in the Pt 4f region and a O 1s component at 529.7 eV.

The O 1s spectrum for the 0.61 ML film [panel (a)] exhibits three components as expected for trilayer FeO$_2$, including the surface (grey) and interface (orange) O peaks. The black component has a binding energy of 529.7 eV, which is similar to the binding energy found for O/Pt [cf. Figure 4.3(b)]. Therefore, the black component at 529.7 eV is assigned to O adsorbed on the uncovered Pt(111) surface, as expected from the p(2x2) symmetry found using LEED [cf. Figure 6.6(a)]. It can, however, not be excluded that patches of unoxidised FeO exist on the 0.61 ML FeO$_2$ preparation. As shown in Figure 6.7(d) such unoxidesed patches lead to a O 1s component at 529.4 eV and it is thus difficult to deconvolute this feature, from the nearby (2x2)-O/Pt component.

The Pt 4f spectrum shown in panel (b) exhibits three components for each spin-orbit split level. The blue components are attributed to bulk Pt atoms and the orange components are assigned to the Pt atoms interfacing with FeO$_2$ in accordance with the 1 ML case [panel (e)]. The third component pair (green) has binding energies of 73.8 eV and 70.4 eV, which is the same as for surface Pt atoms [cf. Figure 4.2(a) and Figure 4.3(a)]. Therefore, the green components are assigned to surface Pt atoms that do not bind to O atoms in a p(2x2)-O structure [the grey atoms in Figure 4.2(b)].

In the Fe 3p signal a difference in peak intensity is seen between the two preparations, cf. Figure 6.8 (c) and (f). As the 1 ML contains more Fe atoms a larger Fe 3p signal is observed with respect to Pt 4f.

Comparing the core level binding energies for the different preparations it is evident that no large differences are observed. The O 1s spectra indicates a difference in binding energy for the different preparations. The surface and interface O is shifted +0.12 eV and -0.18 eV, respectively, for the 1 Ml
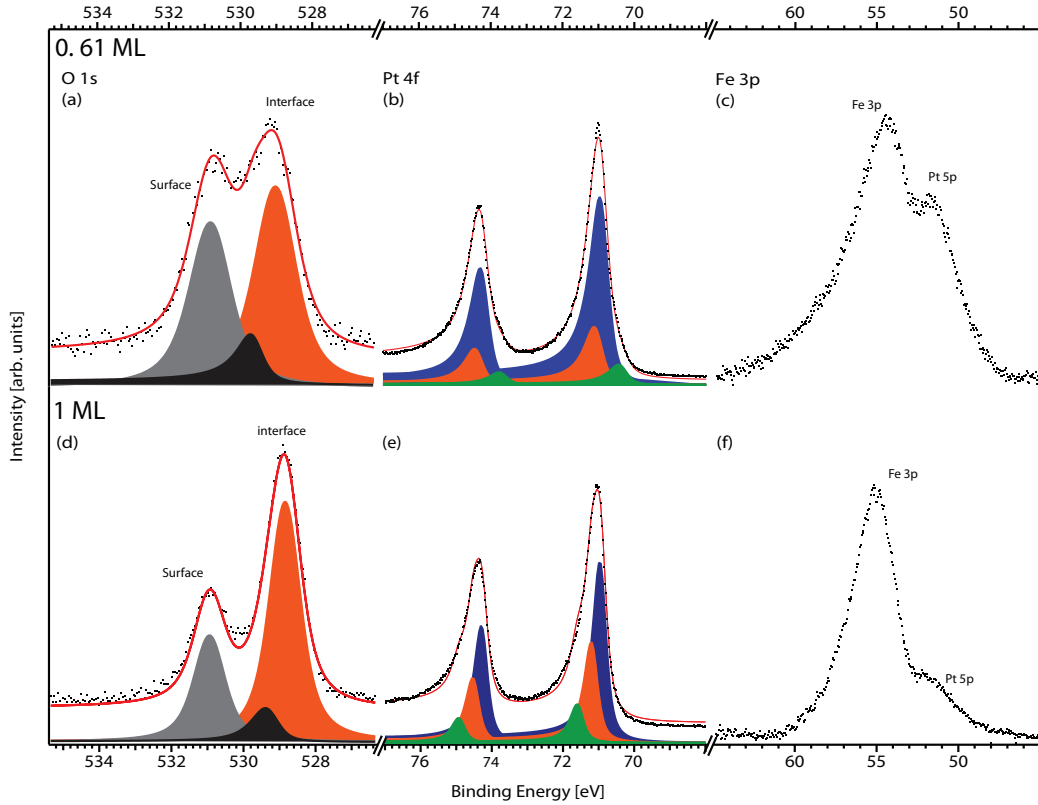
Fig. 6.8: Core level spectra for the two different preparations measured in UHV after high pressure treatment. The top spectra are for the 0.61 ML FeO$_2$ film, the three lower spectra are for the 1 ML FeO$_2$ surface.

case compared to the 0.61 ML preparation. Also, the peaks for 0.61 ML are broader than for 1 ML, Γ_G=0.59 eV and Γ_G= 0.5 eV, respectively. The trilayer oxidation is reported to be site-specific [66], which means that the 0.61 FeO film could form fully oxidised FeO$_2$ islands at the on top symmetry regions. This could result in an alternative structure compared to the 1 ML film and a different unit cell, which can yield different peak widths.

The most pronounced difference between the preparations is the ratio between surface and interface O in the O 1s signal. For the 0.61 ML film it seems like there is an almost equal ratio between the area of the surface and interface peaks, while for the 1 ML spectra the area of the interface peak is much larger than for the surface O peak. The difference in ratio may be a result of the formation of a buckled structure of FeO$_2$ as proposed by Giordano et al. [65]. In this structure, the surface O is ordered according to a ($\sqrt{3}$x$\sqrt{3}$)R30° symmetry. Further, the structure contains only 1/3 of the O atoms compared to FeO, while the interface layer contains as much oxygen as

Tab. 6.1: Binding energies for some of the peaks in Figure 6.8.

Peak	0.61 ML	1 ML
O 1s		
Surface [eV]	530.82	530.94
Interface [eV]	529.03	528.85
Pt 4f$_{7/2}$		
Bulk [eV]	70.44	70.44
Pt interface[eV]	71.12	71.21

the FeO bilayer does. Altogether, this implies a FeO$_{1.3}$ stochiometry. However, Giordano et al. also performed a *thermal desorption spectroscopy* study, which revealed two desorption peaks with an almost 1:1 ratio, one at ~840 K and the other at ~1170 K [65]. The latter peak was said to be virtually identical to a desorption peak obtained from bilayer FeO(111) and thus the peak at ~840 K must originate from the trilayer, which is reduced back into a bilayer. The measured 1:1 ratio suggests a film with a FeO$_2$ stochiometry, which implies that: (i) the interface layer contains more O atoms than the surface layer, and (ii) the interface layer O atoms are more closely packed compared to the O atoms in bilayer FeO(111), which can explain the ratio difference observed for the 1 ML film [cf. Figure 6.8(d)]. However, for the 0.61 ML preparation the surface/interface O ratio is near one. Therefore, the criteria for the buckled structure are not fulfilled for the 0.61 ML film suggesting a coverage dependent structure, at least for subML to ML coverages. As it is extremely difficult to extract structural information from my XPS experiments, no conclusion may be drawn about the reason for different intensities in the O 1s spectrum between the 0.61 ML and 1 ML films. In order to address this issue, further studies are needed with both XPS and complementary methods, like STM, which can account for structural information.

The Pt 4f spectra are almost identical for the 0.61 ML and the 1 ML film. The ratio between the orange Pt-FeO2 interface component and the blue Pt bulk component is different for the the two preparations, which is expected due to the increased amount of FeO$_2$. The orange interface components are shifted slightly (0.09 eV) for the 1 ML film compared to the 0.61 ML film, which is explained by the difference between the layers as discussed above.

In conclusion, only small differences in the core level spectra of the two FeO$_2$ coverages could be detected with XPS. Some shifts in the O 1s lines were seen, but the major difference is the surface/interface O peak ratio. Due to lack of structural information in the XPS data, no conclusion for the underlying

reason for the ratio difference can be drawn and further study is required.

6.6 Reactivity measurements

Reactivity measurement were performed in order to directly study the suggested oxidation of CO, but unfortunately no reaction was observed. The reason for this is unknown and further tests are required. The oxidation method in literature has been in batch mode with relatively high CO pressures, 10 mbar. The HPXPS instrument used cannot use batch mode as the HP cell is pumped constantly by the prelens via the cell aperture nozzle. Furthermore, the maximum pressure used was 0.28 mbar, which is lower than that used in literature. Therefore the produced CO$_2$ concentration might have been below the detection limit in my experiments.

7. Conclusions

A new experiment station has been installed at beamline I511 at the MAX II electron storage ring at the MAX IV Laboratory, and here it has been described in detail. An ultra thin film of FeO was chosen as a test system. The FeO film was oxidised in high pressure of oxygen and *in situ* HPXPS measurements were performed simultaneously. Upon oxidation an additional peak at the high energy side of the original O peak of FeO developed. Further, a small shift in the original O 1s peak position was observed. Using angle resolved XPS, the new component was assigned to the oxygen in the surface layer, while the slightly shifted peak was assigned to the oxygen atoms sandwiched between the Fe and underlying Pt layer. In conclusion the O 1s double peak structure is assigned to the previously reported FeO_2 structure, and this is, according to my knowledge, the first time that the growth of a trilayer FeO_2 film has been observed *in situ*.

The experiment was conducted for two different FeO coverages, 0.61 ML and 1 ML. These film were then oxidised in the same fashion and the peak ratio in the O 1s signal seem to be coverage dependent. Further study with a complementary technique, such as STM, would be helpful in understanding the difference. Altogether, the XPS fingerprint of trilayer FeO_2 has been identified and a repeatable method for growing the film has been used.

The above described conclusions clearly demonstrates the ability to perform *in situ* HPXPS measurements. Reactivity measurements of CO oxidation over Pt(111) were conducted to test the QMS setup. The reaction could be detected by the QMS and in the HPXP spectra. In contrast, no reactivity could be seen for CO oxidation over the FeO_2 film grown on Pt(111). The absence of observed CO oxidation reactivity is in contrast to what have been reported in the literature. Pressure limitations in the experimental setup and the use of flow mode is used to explain the absence of CO oxidation reactivity in my experiments.

Outlook

The study of trilayer FeO_2 holds many possibilities. For example it may be used as a nanoparticle support for catalysis. Additional experiments that could be performed are oxidation reactions of other molecules. A previously used example is styrene epoxidation. Normally styrene is adsorbed onto a surface and can thus be detected easily by XPS, however, styrene epoxide usually desorbs. With the HPXS instrument, it would be possible to simultaneously detect the gas phase styrene epoxide as well as the adsorbed styrene while performing coincidence QMS measurements.

Currently a new cell for the HPXPS instrument is being developed. The new cell will make it possible to study the gas-liquid interface and will hopefully become operational later this year. Additionally, in 2013 the beamline will be exchanged as part of the SPECIES project. This means that the problem with de-focused light spot will vanish and the transmission will increase, opening up for higher pressures.

Bibliography

[1] V. Smil, "Detonator of the population explosion," *Nature*, vol. 400, no. 6743, p. 415, 1999.

[2] http://www.nobelprize.org/nobel_prizes/chemistry/laureates/1918/.

[3] http://www.nobelprize.org/nobel_prizes/chemistry/laureates/1931/.

[4] http://www.nobelprize.org/nobel_prizes/chemistry/laureates/2007/.

[5] J. A. Jensen, K. B. Rider, M. Salmeron, and G. A. Somorjai, "High Pressure Adsorbate Structures Studied by Scanning Tunneling Microscopy: CO on Pt(111) in Equilibrium with the Gas Phase," *Phys. Rev. Lett.*, vol. 80, pp. 1228–1231, 1998.

[6] K. B. Rider, K. S. Hwang, M. Salmeron, and G. A. Somorjai, "Structure and Dynamics of Dense Monolayers of NO Adsorbed on Rh(111) in Equilibrium with the Gas Phase in the Torr Pressure Range," *Phys. Rev. Lett.*, vol. 86, p. 4330, 2001.

[7] P. Cernota, K. Rider, H. Yoon, M. Salmeron, and G. Somorjai, "Dense structures formed by CO on Rh(111) studied by scanning tunneling microscopy," *Surf. Sci.*, vol. 445, p. 249, 2000.

[8] L. Österlund, P. B. Rasmussen, P. Thostrup, E. Lægsgaard, I. Stensgaard, and F. Besenbacher, "Bridging the Pressure Gap in Surface Science at the Atomic Level: H/Cu(110)," *Phys. Rev. Lett.*, vol. 86, p. 460, 2001.

[9] K. Siegbahn, C. Nordling, G. Johansson, J. Hedman, P. F. Heden, K. Hamrin, U. Gelius, T. Bergmark, L. O. Werme, R. Manne, and Y. Baer, *ESCA applied to free molecules*. Amsterdam: North-Holland Publ. Co., 1969.

[10] H. Siegbahn and K. Siegbahn, "ESCA applied to liquids," *J. Electron Spectrosc. Relat. Phenom.*, vol. 2, p. 319, 1973.

[11] R. W. Joyner, M. Roberts, and K. Yates, "A "high-pressure" electron spectrometer for surface studies," *Surf. Sci.*, vol. 87, p. 501, 1979.

[12] H. Siegbahn, "Electron spectroscopy for chemical analysis of liquids and solutions," *J. Phys. Chem.*, vol. 89, p. 897, 1985.

[13] D. M. Littrell and B. J. Tatarchuk, "Hydrazine reduction of transition metal oxides: In situ characterization using x-ray photoelectron spectroscopy," *J. Vac. Sci. Technol. A*, vol. 4, p. 1608, 1986.

[14] a. M. G. H. J. Ruppender, K. C. W., and M. Wilmers, "In situ X-ray photoelectron spectroscopy of surfaces at pressures up to 1 mbar," *Surf. Interface Anal.*, vol. 15, p. 245, 1990.

[15] M. Grunze, D. J. Dwyer, M. Nassir, and Y. Tsai, "Controlled-Atmosphere Photoelectron Spectroscopy," in *Surface Science of Catalysis*, ch. 12, Washington, D.C: American Chemical Society, 1992.

[16] D. F. Ogletree, H. Bluhm, G. Lebedev, C. S. Fadley, Z. Hussain, and M. Salmeron, "A differentially pumped electrostatic lens system for photoemission studies in the millibar range," *Rev. Sci. Instrum.*, vol. 73, p. 3872, 2002.

[17] H. Bluhm, M. Hävecker, A. Knop-Gericke, E. Kleimenov, R. Schlögl, D. Teschner, V. Bukhtiyarov, D. Ogletree, and M. Salmeron, "Methanol oxidation on a copper catalyst investigated using in situ X-ray photoelectron spectroscopy," *J. Phys. Chem. B*, vol. 108, p. 14340, 2004.

[18] D. F. Ogletree, H. Bluhm, E. D. Hebenstreit, and M. Salmeron, "Photoelectron spectroscopy under ambient pressure and temperature conditions," *Nucl. Instrum. Meth. A*, vol. 601, p. 151, 2009.

[19] J. Schnadt, J. Knudsen, J. N. Andersen, H. Siegbahn, A. Pietzsch, F. Hennies, N. Johansson, N. Martensson, G. Ohrwall, S. Bahr, S. Mahl, and O. Schaf, "The New Near-Ambient Pressure X-ray Photoelectron Spectroscopy Instrument at MAX-lab." Submitted to J. Synchrotron Radiat.

[20] H. Hertz, "Ueber einen Einfluss des ultravioletten Lichtes auf die electrische Entladung," *Ann. Phys.*, vol. 267, p. 983, 1887.

[21] A. Einstein, "Ueber einen die Erzeugung und Verwandlung des Lichtes betreffenden heuristischen Gesichtspunkt," *Ann. Phys.*, vol. 322, p. 132, 1905.

[22] S. Hüfner, *Photoelectron Spectroscopy - Principles and Applications.* Berlin: Springer, third ed., 2003.

[23] A. Jablonski, "Effects of Auger electron elastic scattering in quantitative AES," *Surf. Sci.*, vol. 188, p. 164, 1987.

[24] C. Powell, "The quest for universal curves to describe the surface sensitivity of electron spectroscopies," *J. Electron Spectrosc. Relat. Phenom.*, vol. 47, p. 197, 1988.

[25] M. Salmeron and R. Schlögl, "Ambient pressure photoelectron spectroscopy: A new tool for surface science and nanotechnology," *Surf. Sci. Rep.*, vol. 63, p. 169, 2008.

[26] G. Attard and C. Barnes, *Surfaces.* Oxford: Oxford University Press, 1998.

[27] J. Yeh and I. Lindau, "Atomic subshell photoionization cross sections and asymmetry parameters: $1 \leq z \leq 103$," *Atom. Data Nucl. Data*, vol. 32, p. 1, 1985.

[28] J. Cambell and T. Papp, "WIDTHS OF THE ATOMIC K-N7 LEVELS," *Atom.Data Nucl. Data*, vol. 77, p. 1, 2001.

[29] S. Doniach and M. Šunjić, "Many-electron singularity in X-ray photoemission and X-ray line spectra from metals," *J. Phys. C*, vol. 3, p. 285, 1970.

[30] S. Tougaard and B. Jørgensen, "Inelastic background intensities in XPS spectra," *Surf. Sci.*, vol. 143, p. 482, 1984.

[31] D. A. Shirley, "High-Resolution X-Ray Photoemission Spectrum of the Valence Bands of Gold," *Phys. Rev. B*, vol. 5, p. 4709, 1972.

[32] S. Tougaard, "Practical algorithm for background subtraction," *Surf. Sci.*, vol. 216, p. 343, 1989.

[33] G. K. Wertheim, "Determination of the Gaussian and Lorentzian content of experimental line shapes," *Rev. Sci. Instrum.*, vol. 45, p. 1369, 1974.

[34] O. Björneholm, A. Nilsson, H. Tillborg, P. Bennich, A. Sandell, B. Hernnäs, C. Puglia, and N. Mårtensson, "Overlayer structure from adsorbate and substrate core level binding energy shifts: CO, CCH3 and O on Pt(111)," *Surf. Sci.*, vol. 315, p. L983, 1994.

[35] P. Rous, "The tensor LEED approximation and surface crystallography by low-energy electron diffraction," *Prog. Surf. Sci.*, vol. 39, p. 3, 1992.

[36] SPECS GmbH, Berlin, *Optics and Power Supplies ErLEED*, 2003. Technical manual.

[37] R. Denecke, P. Väterlein, M. Bässler, N. Wassdahl, S. Butorin, A. Nilsson, J.-E. Rubensson, J. Nordgren, N. Mårtensson, and R. Nyholm, "Beamline I511 at MAX II, capabilities and performance," *J. Electron Spectrosc. Relat. Phenom.*, vol. 101-103, p. 971, 1999.

[38] S. Aksela, A. Kivimäki, A. N. de Brito, O.-P. Sairanen, S. Svensson, and J. Väyrynen, "Performance of the modified SX-700 plane grating monochromator at the Finnish beamline in MAX-lab," *Rev. Sci. Instrum.*, vol. 65, p. 831, 1994.

[39] R. Nyholm, J. Andersen, U. Johansson, B. Jensen, and I. Lindau, "Beamline I311 at MAX-LAB: a VUV/soft X-ray undulator beamline for high resolution electron spectroscopy," *Nucl. Instrum. Meth. A*, vol. 467-468, Part 1, p. 520, 2001.

[40] G. Brown, K. Halbach, J. Harris, and H. Winick, "Wiggler and undulator magnets - A review," *Nuclear Instruments and Methods in Physics Research*, vol. 208, p. 65, 1983.

[41] H. Petersen, "The high energy plane grating monochromators at BESSY," *Nuclear Instruments and Methods in Physics Research Section A: Accelerators, Spectrometers, Detectors and Associated Equipment*, vol. 246, p. 260, 1986.

[42] S. Urpelainen, M. Huttula, T. Balasubramanian, R. Sankari, P. Kovala, E. Kukk, E. Nommiste, S. Aksela, R. Nyholm, and H. Aksela, "FINEST: a high performance branch-line for VUV photon energy range gas phase studies at MAX-lab," in *SRI 2009: THE 10TH INTERNATIONAL CONFERENCE ON SYNCHROTRON RADIATION INSTRUMENTATION* (Garrett, R and Gentle, I and Nugent, K and Wilkins, S, ed.), vol. 1234 of *AIP Conference Proceedings*, pp. 411–414, 2010.

[43] SPECS GmbH, *PHOIBOS NAP Hemispherical Energy Analyzer Series Near Ambient Pressure Analyzer*, 2010. Technical Manual.

[44] B. Henke, E. Gullikson, and J. Davis, "X-Ray Interactions: Photoabsorption, Scattering, Transmission, and Reflection at E = 50-30,000 eV, Z = 1-92," *Atom. Data Nucl. Data*, vol. 54, p. 181, 1993.

[45] http://henke.lbl.gov/optical_constants/.

[46] H. Bluhm, M. Hävecker, A. Knop-Gericke, M. Kiskinova, R. Schlögl, and M. Salmeron, "In Situ X-Ray Photoelectron Spectroscopy Studies

of Gas-Solid Interfaces at Near-Ambient Conditions," *MRS Bull.*, vol. 32, no. 12, p. 1022, 2007.

[47] SPECS GmbH, *XR50 X-ray Source*, 2009. Technical Manual.

[48] www.pall.com.

[49] SPECS GmbH, *PureGas 3 Computerized Multigas Inlet Panel*, 2011. Technical Manual.

[50] Brooks Instrument, *Brooks GF Series High Performance Gas Flow Controllers*, 2010. Technical Manual.

[51] AMETEK Process Instruments, *Dycor LC-D Residual Gas Analyzer*, 2004. Technical Manual.

[52] H. Steininger, S. Lehwald, and H. Ibach, "On the adsorption of CO on Pt(111) ," *Surf. Sci.*, vol. 123, p. 264, 1982.

[53] I. Langmuir, "The mechanism of the catalytic action of platinum in the reactions $2CO + O_2 = 2CO_2$ and $2H_2 + O_2 = 2H_2O$," *Trans. Faraday Soc.*, vol. 17, p. 621, 1922.

[54] T. Engel and G. Ertl, "Elementary Steps in the Catalytic Oxidation of Carbon Monoxide on Platinum Metals," vol. 28 of *Advances in Catalysis*, pp. 1 – 78, Waltham: Academic Press, 1979.

[55] X. Su, P. S. Cremer, Y. R. Shen, and G. A. Somorjai, "High-Pressure CO Oxidation on Pt(111) Monitored with Infrared-Visible Sum Frequency Generation (SFG)," *J. Am. Chem. Soc.*, vol. 119, p. 3994, 1997.

[56] G. Vurens, M. Salmeron, and G. Somorjai, "Structure, composition and chemisorption studies of thin ordered iron oxide films on platinum (111)," *Surf. Sci.*, vol. 201, p. 129, 1988.

[57] J. Knudsen, L. R. Merte, L. C. Grabow, F. M. Eichhorn, S. Porsgaard, H. Zeuthen, R. T. Vang, E. Lægsgaard, M. Mavrikakis, and F. Besenbacher, "Reduction of FeO/Pt(111) thin films by exposure to atomic hydrogen," *Surf. Sci.*, vol. 604, p. 11, 2010.

[58] H. Galloway, J. Benítez, and M. Salmeron, "The structure of monolayer films of FeO on Pt(111) ," *Surf. Sci.*, vol. 298, p. 127, 1993.

[59] Y.-N. Sun, Z.-H. Qin, M. Lewandowski, E. Carrasco, M. Sterrer, S. Shaikhutdinov, and H.-J. Freund, "Monolayer iron oxide film on platinum promotes low temperature CO oxidation," *J. Catal.*, vol. 266, p. 359, 2009.

[60] W. Weiss and W. Ranke, "Surface chemistry and catalysis on well-defined epitaxial iron-oxide layers," *Prog. Surf. Sci.*, vol. 70, p. 1, 2002.

[61] Y. J. Kim, C. Westphal, R. X. Ynzunza, H. C. Galloway, M. Salmeron, M. A. Van Hove, and C. S. Fadley, "Interlayer interactions in epitaxial oxide growth: FeO on Pt(111)," *Phys. Rev. B*, vol. 55, p. R13448, 1997.

[62] W. Ranke, M. Ritter, and W. Weiss, "Crystal structures and growth mechanism for ultrathin films of ionic compound materials: FeO(111) on Pt(111)," *Phys. Rev. B*, vol. 60, p. 1527, 1999.

[63] S. R. Longwitz, J. Schnadt, E. K. Vestergaard, R. T. Vang, I. Stensgaard, H. Brune, and F. Besenbacher, "High-Coverage Structures of Carbon Monoxide Adsorbed on Pt(111) Studied by High-Pressure Scanning Tunneling Microscopy," *J. Phys. Chem. B*, vol. 108, p. 14497, 2004.

[64] D. Miller, S. K. H. Öberg, H. S. Casalongue, D. Friebel, T. Anniyev, H. Ogasawara, H. Bluhm, L. Pettersson, and A. Nilsson, "Oxidation of Pt(111) under Near-Ambient Conditions," *Phys. Rev. Lett.*, vol. 107, 2011.

[65] L. Giordano, M. Lewandowski, I. M. N. Groot, Y.-N. Sun, J. Goniakowski, C. Noguera, S. Shaikhutdinov, G. Pacchioni, and H.-J. Freund, "Oxygen-Induced Transformations of an FeO(111) Film on Pt(111): A Combined DFT and STM Study," *J. Phys. Chem. C*, vol. 114, p. 21504, 2010.

[66] M. Lewandowski, I. Groot, S. Shaikhutdinov, and H.-J. Freund, "Scanning tunneling microscopy evidence for the Mars-van Krevelen type mechanism of low temperature CO oxidation on an FeO(111) film on Pt(111)," *Catal. Today*, vol. 181, p. 52, 2012.

[67] L. Giordano, G. Pacchioni, J. Goniakowski, N. Nilius, E. D. L. Rienks, and H.-J. Freund, "Interplay between structural, magnetic, and electronic properties in a FeO/Pt(111) ultrathin film," *Phys. Rev. B*, vol. 76, p. 075416, 2007.

[68] Y.-N. Sun, L. Giordano, J. Goniakowski, M. Lewandowski, Z.-H. Qin, C. Noguera, S. Shaikhutdinov, G. Pacchioni, and H.-J. Freund, "The Interplay between Structure and CO Oxidation Catalysis on Metal-Supported Ultrathin Oxide Films," *Angew. Chem. Int. Ed.*, vol. 49, p. 4418, 2010.

[69] J. Gustafson, A. Mikkelsen, M. Borg, J. Andersen, E. Lundgren, C. Klein, W. Hofer, M. Schmid, P. Varga, L. Köhler, G. Kresse,

N. Kasper, A. Stierle, and H. Dosch, "Structure of a thin oxide film on Rh(100)," *Phys. Rev. B*, vol. 71, 2005.